Chapter 3
Breakdown Voltage

The most unique feature of power semiconductor devices is their ability to withstand high voltages. In transistors designed for microprocessors and semiconductor memories, the pressure to reduce their size in order to integrate more devices on a monolithic chip has resulted in a reduction in their operating voltage. In contrast, the desire to control larger power levels in motor drive and power distribution systems has encouraged the development of power devices with larger breakdown voltages. Typical applications for power devices were illustrated in Fig. 1.2. Depending upon the application, the breakdown voltage of devices can range from 20 to 30 V for voltage regulator modules (power supplies) used to deliver power to microprocessors in personal computers and servers to over 5000 V for devices used in power transmission networks.

In this chapter, the physics of avalanche breakdown is analyzed in relation to the properties of the semiconductor region that is supporting the voltage. After treating the one-dimensional junction, the edge terminations for power devices are described. Power devices require special edge terminations due to their finite area. The electric field at the edges usually becomes larger than in the middle of the device leading to a reduction of the breakdown voltage. Significant effort has been undertaken to develop a good understanding of the electric field enhancement at the edges, and methods have been proposed to mitigate the increase in the electric field. Various edge termination approaches are discussed in detail in the chapter because of their importance to maximizing the performance of power devices.

In a semiconductor, the ability to support high voltages without the onset of significant current flow is limited by the avalanche breakdown phenomenon, which is dependent on the electric field distribution within the structure. High electric fields can be created within the interior of power devices as well as at their edges. The design optimization of power devices must be performed to meet the breakdown voltage requirements for the application while minimizing the on-state voltage drop so that the power dissipation is reduced.

Power devices are designed to support high voltages within a depletion layer formed across either a P-N junction, a metal-semiconductor (Schottky barrier)

© Springer International Publishing AG, part of Springer Nature 2019

B. J. Baliga, *Fundamentals of Power Semiconductor Devices*,
https://doi.org/10.1007/978-3-319-93988-9_3

contact, or a metal-oxide-semiconductor (MOS) interface. Any electrons or holes that enter the depletion layer either due to the space charge generation phenomenon or by diffusion from adjacent quasi-neutral regions are swept out by the electric field produced in the region by the applied voltage. As the applied voltage is increased, the electric field in the depletion region increases resulting in acceleration of the mobile carriers to higher velocities. In the case of silicon, the mobile carriers attain a saturated drift velocity of 1×10^7 cm/s when the electric field exceeds 1×10^5 V/cm as discussed in the previous chapter. With further increase in the electric field, the mobile carriers gain sufficient kinetic energy from the electric field so that their interaction with the lattice atoms produces the excitation of electrons from the valence band into the conduction band. The generation of electron-hole pairs due to energy acquired from the electric field in the semiconductor is referred to as *impact ionization*. Since the electron-hole pairs created by impact ionization also undergo acceleration by the electric field in the depletion region, they participate in the creation of further pairs of electrons and holes. Consequently, impact ionization is a multiplicative phenomenon which produces a cascade of mobile carriers being transported through the depletion region leading to a significant current flow through it. Since the device is unable to sustain the application of higher voltages due to a rapid increase in the current, it is considered to undergo *avalanche breakdown*. Thus, avalanche breakdown limits the maximum operating voltage for power devices.

3.1 Avalanche Breakdown

The maximum voltage that can be supported by a power device before the onset of significant current flow is limited by the avalanche breakdown phenomenon. In power devices, the voltage is supported across depletion regions. As discussed in Chap. 2, mobile carriers are accelerated in the presence of a high electric field until they gain sufficient energy to create hole-electron pairs upon collision with the lattice atoms. This impact ionization process determines the current flowing through the depletion region in the presence of a large electric field. An impact ionization coefficient was defined in Chap. 2 as the number of electron-hole pairs created by a mobile carrier traversing 1 cm through the depletion region along the direction of the electric field. The impact ionization coefficients for electrons and holes are a strong function of the magnitude of the electric field as shown in Fig. 2.10.

3.1.1 Power Law Approximations for the Impact Ionization Coefficients

It is convenient to use a power law for the impact ionization coefficients when performing analytical derivations pertinent to the performance of silicon power

devices even though they actually increase exponentially with increasing electric field, as shown in Fig. 2.10. A Fulop's power law approximation (α_F) that was originally proposed for silicon [1] is given by:

$$\alpha_F(\text{Si}) = 1.8 \times 10^{-35} E^7$$
$$\alpha_B(\text{Si}) = 3.507 \times 10^{-35} E^7 \quad (3.1)$$

The impact ionization coefficients obtained by using Fulop's approximation are shown in Fig. 3.1 by the green dashed line together with the impact ionization coefficient for electrons and holes in silicon as governed by Chynoweth's law (shown by the red and blue lines) obtained from measured data. It can be observed that the values obtained using Fulop's power law are significantly smaller than that measured for electrons. This results in analytical solutions for breakdown voltage that are much larger than those actually observed in silicon devices.

Baliga's power law (α_B) for impact ionization coefficients for silicon, also given in Eq. (3.1), was proposed [2] to allow a more accurate analytical computation of the breakdown voltage for silicon devices. The impact ionization coefficients obtained by using Baliga's approximation are shown in Fig. 3.1 by the purple dashed line. It can be observed that the values obtained using Baliga's power law are closer to those measured for electrons in silicon. This allows accurate analytical calculation of the breakdown voltage in silicon power devices.

In the same manner, it is convenient to use Baliga's power law approximation [3] for the impact ionization coefficients for 4H-SiC for analytical derivations:

$$\alpha_B(\text{4H-SiC}) = 3.9 \times 10^{-42} E^7 \quad (3.2)$$

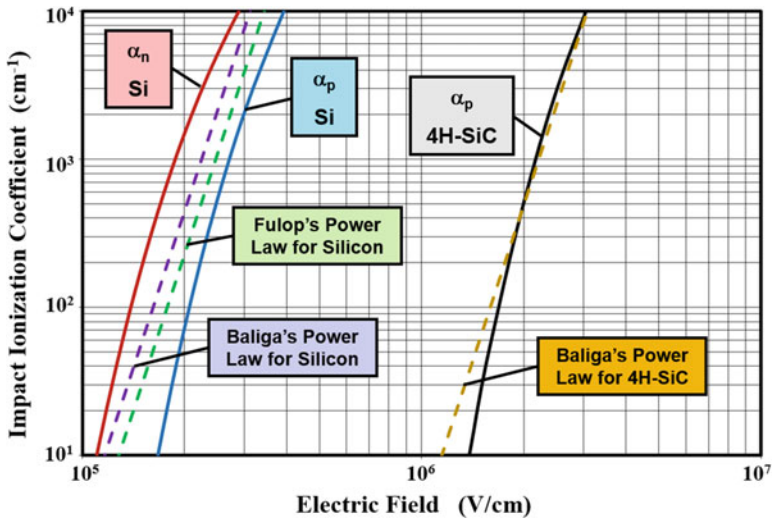

Fig. 3.1 Power law approximations for the impact ionization coefficients in silicon and 4H-SiC

The impact ionization coefficient obtained by using this approximation is also shown in Fig. 3.1 by the brown dashed line together with the impact ionization coefficient for holes in 4H-SiC as governed by Chynoweth's law (based up on data reported by Raghunathan and Baliga [4]). This analytical formulation allows accurate computation of breakdown in 4H-SiC power devices made from material free of defects.

During numerical simulations of power device structures, it is customary to use Chynoweth's formula for the impact ionization coefficients. However, the power law approximations discussed here are valuable for obtaining analytical solutions for the breakdown voltage of planar one-dimensional junctions and the influence of various edge terminations on the breakdown voltage. These analytical solutions provide insight into the physics determining the breakdown phenomenon enabling the design of improved device structures.

3.1.2 Multiplication Coefficient

The avalanche breakdown condition for a diode is defined by the impact ionization rate becoming infinite. In order to analyze this, consider a one-dimensional reverse biased N^+/P junction with a depletion region extending primarily in the P-region. If an electron-hole pair is generated at a distance x from the junction, the hole will be swept toward the contact to the P-region, while the electron is simultaneously swept toward to the junction with the N^+ region. If the electric field in the depletion region is large, these carriers will be accelerated until they gain sufficient energy to create electron-hole pairs during collisions with the lattice atoms. Based upon the definitions for the impact ionization coefficients, the hole will create $[\alpha_p dx]$ electron-hole pairs when traversing a distance dx through the depletion region. Simultaneously, the electron will create $[\alpha_n dx]$ electron-hole pairs when traversing a distance dx through the depletion region. The total number of electron-hole pairs created in the depletion region due to a single electron-hole pair initially generated at a distance x from the junction is given by [5, 6]:

$$M(x) = 1 + \int_0^x \alpha_n M(x) dx + \int_x^W \alpha_p M(x) dx \tag{3.3}$$

where W is the width of the depletion layer. A solution for this equation is given by:

$$M(x) = M(0) \exp\left[\int_0^x (\alpha_n - \alpha_p) dx\right] \tag{3.4}$$

where $M(0)$ is the total number of electron-hole pairs at the edge of the depletion region. Using this expression in Eq. (3.3) with $x = 0$ provides a solution for $M(0)$:

$$M(0) = \left\{1 - \int_0^W \alpha_p \exp\left[\int_0^x (\alpha_n - \alpha_p)dx\right]dx\right\}^{-1} \tag{3.5}$$

Using this expression in Eq. (3.4) gives:

$$M(x) = \frac{\exp\left[\int_0^x (\alpha_n - \alpha_p)dx\right]}{1 - \int_0^W \alpha_p \exp\left[\int_0^x (\alpha_n - \alpha_p)dx\right]dx} \tag{3.6}$$

This expression for $M(x)$, referred to as the *multiplication coefficient*, allows calculation of the total number of electron-holes pairs created as a result of the generation of a single electron-hole pair at a distance x from the junction if the electric field distribution along the impact ionization path is known. The avalanche breakdown condition, defined to occur when the total number of electron-hole pairs generated within the depletion region approaches infinity, corresponds to M becoming equal to infinity. This condition is attained by setting the denominator of Eq. (3.6) to zero:

$$\left\{\int_0^W \alpha_p \exp\left[\int_0^x (\alpha_n - \alpha_p)dx\right]dx\right\} = 1 \tag{3.7}$$

The expression on the left-hand side of Eq. (3.7) is known as the *ionization integral*. During the analysis of avalanche breakdown in power devices, it is common practice to find the voltage at which the ionization integral becomes equal to unity. If the impact ionization coefficients for electrons and holes are assumed to be equal, the avalanche breakdown condition can be written as:

$$\int_0^W \alpha dx = 1 \tag{3.8}$$

This approach to the determination of the breakdown voltage is valid for power rectifiers and MOSFETs where the current flowing through the depletion region is not amplified. In devices, such as thyristors and IGBTs, the current flowing through the depletion region becomes amplified by the gain of the internal transistors. In these cases, it becomes necessary to solve for the multiplication coefficient instead of using the ionization integral as discussed later.

The multiplication coefficient for a high-voltage P^+/N diode is given by [7]:

$$M_p = \frac{1}{1 - (V/\mathrm{BV})^6} \tag{3.9}$$

where V is the applied reverse bias voltage and BV is the breakdown voltage, while that for a N^+/P diode is given by:

$$M_n = \frac{1}{1 - (V/\mathrm{BV})^4} \tag{3.10}$$

Thus, the reverse current for a P^+/N diode approaches infinity at a faster rate with increasing voltage than for a N^+/P diode. This has been related to the diffusion current due to holes from the N-region in the P^+/N diode.

3.2 Abrupt One-Dimensional Diode

Power devices are designed to support high voltages across a depletion layer formed at either a P-N junction, a metal-semiconductor (Schottky barrier) contact, or a metal-oxide-semiconductor (MOS) interface. The onset of the avalanche breakdown condition can be analyzed for all these cases by assuming the voltage is supported across only one side of the structure. This holds true for an abrupt P-N junction with a very high doping concentration on one side when compared with the other side. In junctions formed with a shallow depth and a high surface concentration with a lightly doped underlying region of opposite conductivity type, the depletion region extends primarily in the lightly doped region allowing their treatment as abrupt junctions.

The analysis of a one-dimensional abrupt junction can be used to understand the design of the drift region within power devices. The case of a P^+/N junction is illustrated in Fig. 3.2 where the P^+ side is assumed to be very highly doped so that the electric field supported within it can be neglected. When this junction is reverse biased by the application of a positive bias to the N-region, a depletion region is formed in the N-region together with the generation of a strong electric field within it that supports the voltage. Poisson's equation for the N-region is then given by:

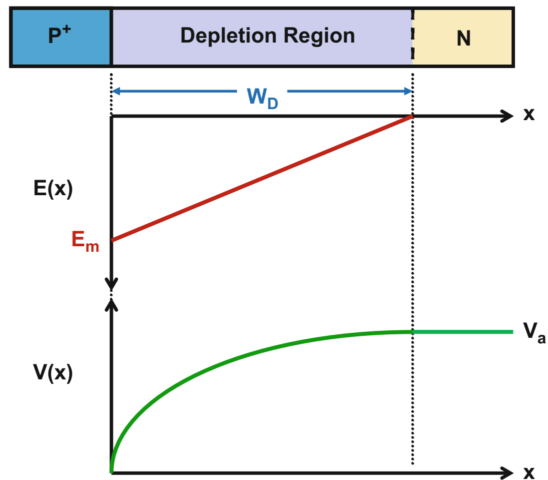

Fig. 3.2 Electric field and potential distribution for an abrupt parallel-plane P^+N junction

$$\frac{d^2V}{dx^2} = -\frac{dE}{dx} = -\frac{Q(x)}{\varepsilon_S} = -\frac{qN_D}{\varepsilon_S} \tag{3.11}$$

where $Q(x)$ is the charge within the depletion region due to the presence of ionized donors, ε_S is the dielectric constant for the semiconductor, q is the electron charge, and N_D is the donor concentration in the uniformly doped N-region.

Integration of the above equation with the boundary condition that the electric field must go to zero at the edge of the depletion region (i.e., at $x = W_D$) provides the electric field distribution:

$$E(x) = -\frac{qN_D}{\varepsilon_S}(W_D - x) \tag{3.12}$$

The electric field has a maximum value of E_m at the P^+/N junction ($x = 0$) and decreases linearly to zero at $x = W_D$. Integration of the electric field distribution through the depletion region provides the potential distribution:

$$V(x) = \frac{qN_D}{\varepsilon_S}\left(W_D x - \frac{x^2}{2}\right) \tag{3.13}$$

This equation is obtained by using the boundary condition that the potential is zero at $x = 0$ within the P^+ region. The potential varies quadratically as illustrated in the figure.

By using the boundary condition:

$$V(W_D) = V_a \tag{3.14}$$

the thickness of the depletion region (W_D) can be related to the applied reverse bias (V_a):

$$W_D = \sqrt{\frac{2\varepsilon_S V_a}{qN_D}} \tag{3.15}$$

Using these equations, the maximum electric field at the junction can be obtained:

$$E_m = \sqrt{\frac{2qN_D V_a}{\varepsilon_S}} \tag{3.16}$$

When the applied bias increases, the maximum electric field approaches values at which significant impact ionization begins to occur. The breakdown voltage is determined by the ionization integral becoming equal to unity:

$$\int_0^W \alpha . dx = 1 \tag{3.17}$$

where α is the impact ionization coefficient discussed in Chap. 2. In order to obtain a closed form solution for the breakdown voltage, it is convenient to use the power law for the impact ionization coefficient in place of Chynoweth's law. Substituting Baliga's power law for silicon into Eq. (3.17) with the electric field distribution given by Eq. (3.12), analytical solutions for the breakdown voltage and the corresponding maximum depletion layer width can be derived for silicon:

$$\mathrm{BV_{PP}(Si)} = 4.45 \times 10^{13} N_D^{-3/4} \tag{3.18}$$

and

$$W_{\mathrm{PP}}(\mathrm{Si}) = 2.404 \times 10^{10} N_D^{-7/8} \tag{3.19}$$

In a similar manner, substituting Baliga's power law for 4H-SiC into Eq. (3.17) with the electric field distribution given by Eq. (3.12), analytical solutions for the breakdown voltage and the corresponding maximum depletion layer width can be derived for 4H-SiC:

$$\mathrm{BV_{PP}(4H\text{-}SiC)} = 3.0 \times 10^{15} N_D^{-3/4} \tag{3.20}$$

and

$$W_{\mathrm{PP}}(\mathrm{4H\text{-}SiC}) = 1.82 \times 10^{11} N_D^{-7/8} \tag{3.21}$$

The breakdown voltages predicted by the analytical solutions are plotted in Fig. 3.3 as a function of the doping concentration on the lightly doped side of the junction. It can be seen that the breakdown voltage decreases with increasing doping

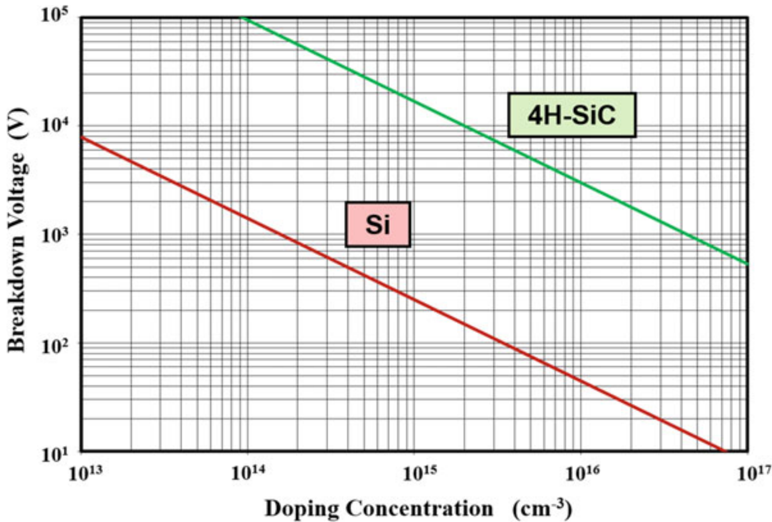

Fig. 3.3 Breakdown voltage for abrupt parallel-plane junctions in Si and 4H-SiC

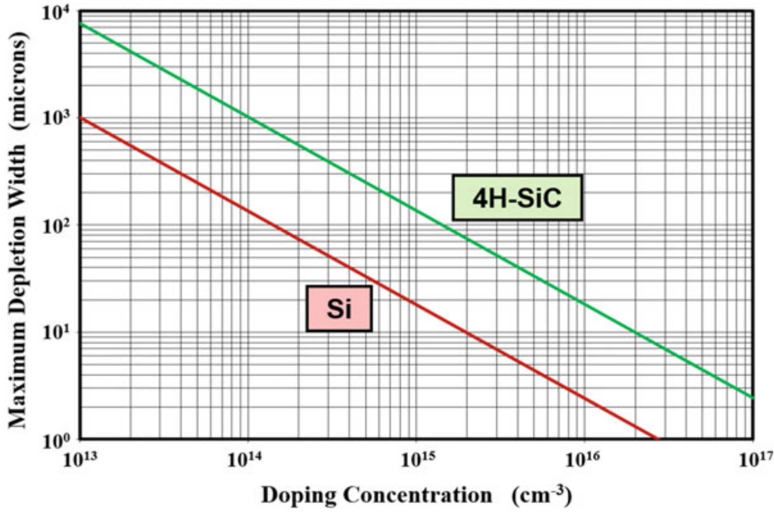

Fig. 3.4 Maximum depletion width at breakdown in Si and 4H-SiC

concentration. It is worth pointing out that it is possible to support a much larger voltage in 4H-SiC when compared with silicon for any given doping concentration. The ratio of the breakdown voltage in 4H-SiC to that in silicon for the same doping concentration is found to be 67.4. It is also obvious from this figure that for a given breakdown voltage, it is possible to use a much higher doping concentration in the drift region for 4H-SiC devices when compared with silicon devices. The ratio of the doping concentration in the drift region for a 4H-SiC device to that for a silicon device with the same breakdown voltage is found to be 274.

The maximum depletion width reached at the onset of breakdown is shown in Fig. 3.4 for silicon and 4H-SiC. It can be seen that the thickness of the lightly doped side of the junction must be increased as the doping level is reduced in order to support larger voltages. For the same doping concentration, the maximum depletion width in 4H-SiC is 7.57 times larger than that in silicon because it can sustain a much larger electric field. However, for a given breakdown voltage, the depletion width in 4H-SiC is smaller by a factor of 18 times compared with a silicon device because of the much larger doping concentration in the drift region. This smaller depletion width, in conjunction with the far larger doping concentration, results in an enormous reduction in the specific on-resistance of the drift region in 4H-SiC when compared with silicon.

The onset of the avalanche breakdown for an abrupt parallel-plane junction, as defined by the above equations, is accompanied by a maximum electric field at the junction referred to as the *critical electric field* for breakdown. Combining Eqs. (3.16) and (3.18), the critical electric field for breakdown in silicon is given by:

$$E_C(\mathrm{Si}) = 3700 N_D^{1/8} \tag{3.22}$$

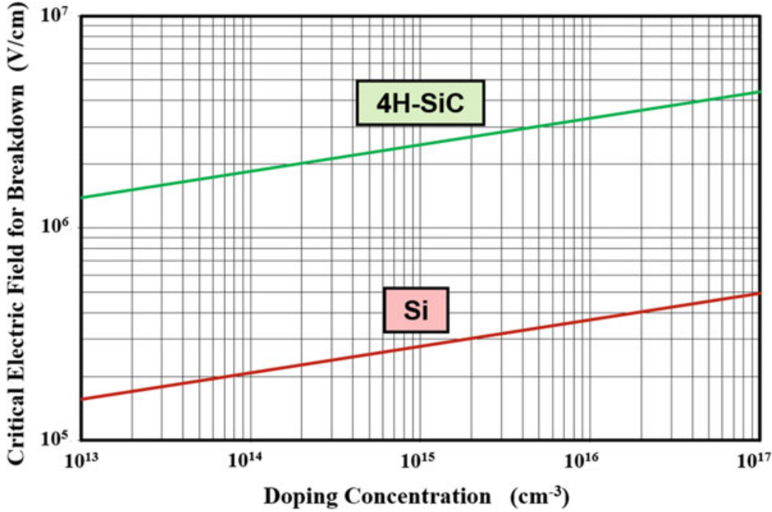

Fig. 3.5 Critical electric field for breakdown in Si and 4H-SiC

while that for 4H-SiC is given by:

$$E_C(\text{4H-SiC}) = 33,000 N_D^{1/8} \tag{3.23}$$

The critical electric field for 4H-SiC can be compared with that for silicon in Fig. 3.5. In both cases, the critical electric field is a weak function of the doping concentration. The critical electric field in 4H-SiC is 8.92× larger than in silicon for the same doping concentration. The larger critical electric field in 4H-SiC results in a much larger *Baliga's figure of merit* (see Chap. 1).

The critical electric field is a useful parameter for identifying the onset of avalanche breakdown in power device structures. Due to the very strong dependence of the impact ionization coefficients on the electric field strength, avalanche breakdown can be usually assumed to occur when the electric field within any local region of a power device approaches the critical electric field. However, it is important to note that this provides only an indication of the onset of breakdown and the exact breakdown voltage must be determined by extracting the ionization integral. This is particularly true for devices where the electric field deviates from the triangular shape pertinent to an abrupt parallel-plane junction.

3.2.1 Temperature Dependence

The mean free path for electron and hole transport becomes shorter with increasing temperature due to enhanced scattering of the carriers. Consequently, the carriers gain less energy from the electric field at elevated temperatures. Consequently, the

impact ionization coefficients for electrons and holes decrease with increasing temperature. This produces an increase in the avalanche breakdown voltage at the rate of 0.454 V/°C in silicon power devices which corresponds to about 20% increase from 300 to 500 °K [8].

3.3 Ideal Specific On-Resistance

The specific on-resistance of the drift region is related to the breakdown voltage by Eq. (1.11) which is repeated here for discussion:

$$R_{\mathrm{on,\,sp}} = \frac{4\mathrm{BV}^2}{\varepsilon_{\mathrm{S}}\mu_{\mathrm{n}}E_{\mathrm{C}}^3} \tag{3.24}$$

An accurate modeling of the specific on-resistance requires taking into account the dependence of the critical electric field and mobility on the doping concentration, which varies as the breakdown voltage is changed. It is possible to do this by computing the doping concentration for achieving a given breakdown voltage and then using the equations for the depletion width and mobility as a function of doping concentration to obtain the specific on-resistance:

$$R_{\mathrm{on,\,sp}} = \frac{W_{\mathrm{PP}}}{q\mu_{\mathrm{n}}N_{\mathrm{D}}} \tag{3.25}$$

The specific on-resistance projected for the drift region in 4H-SiC devices by using the above method is compared with that for silicon devices in Fig. 3.6.

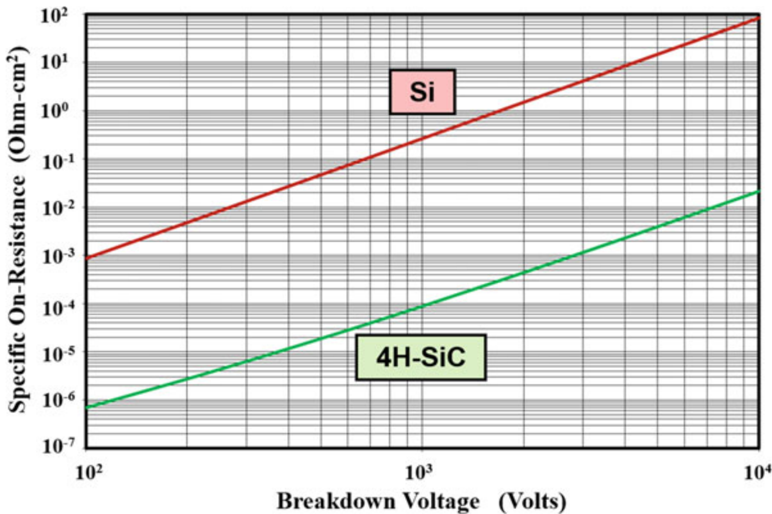

Fig. 3.6 Specific on-resistance of drift regions in 4H-SiC and silicon

The values for 4H-SiC are about 2000 times smaller than for silicon devices for the same breakdown voltage. This has encouraged the development of unipolar power devices [2], such as Schottky rectifiers and MOSFETs, from 4H-SiC. The actual resistance within the structures can be significantly larger than the ideal specific on-resistance as discussed in later chapters.

3.4 Abrupt Punch-Through Diode

In the case of some power devices, such as P-i-N rectifiers, the resistance of the drift region is greatly reduced during on-state current flow by the injection of a large concentration of minority carriers. In these cases, the doping concentration of the drift region does not determine the resistance to the on-state current flow. Consequently, it is preferable to use a thinner depletion region with a reduced doping concentration to support the voltage. This configuration for the drift region is called the *punch-through design*.

The electric field distribution for the punch-through design is shown in Fig. 3.7. In comparison with the triangular electric field distribution shown in Fig. 3.2, the electric field for the punch-through design takes a trapezoidal shape. The electric field varies more gradually through the drift region due to its lower doping concentration and then very rapidly with distance within the N^+ end region due to its very high doping concentration. The electric field at the interface between the drift region and the N^+ end region is given by:

$$E_1 = E_m - \frac{qN_{DP}}{\varepsilon_S} W_{D,PT} \tag{3.26}$$

where E_m is the maximum electric field at the junction, N_{DP} is the doping concentration in the N-type drift region, and $W_{D,PT}$ is the width of the N-type drift region in the punch-through structure.

The voltage supported by the punch-through diode is given by:

$$V_{PT} = \left(\frac{E_m + E_1}{2}\right) W_{D,PT} \tag{3.27}$$

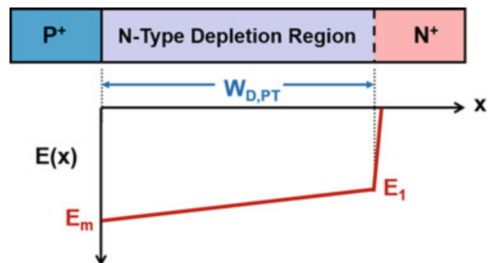

Fig. 3.7 Punch-through design for a P-i-N rectifier

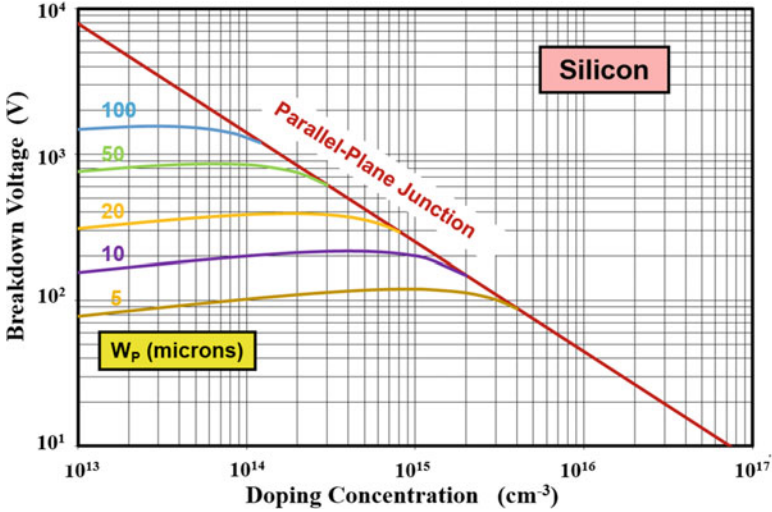

Fig. 3.8 Breakdown voltages for the silicon P-i-N diodes with punch-through design

if the small voltage supported within the N^+ end region is neglected. The punch-through diode undergoes avalanche breakdown when the maximum electric field (E_m) becomes approximately equal to the critical electric field (E_C) for breakdown. Using this condition in Eq. (3.27) together with the field distribution in Eq. (3.26), the breakdown voltage for the punch-through diode is given by:

$$BV_{PT} = E_c W_{D,PT} - \frac{q N_{DP} W_{D,PT}^2}{2\varepsilon_S} \tag{3.28}$$

The breakdown voltages calculated using this relationship are shown in Fig. 3.8 for silicon punch-through diodes with various thicknesses for the drift region. In performing these calculations, the change in the critical electric field with doping concentration was taken into account. For any doping concentration for the drift region, the breakdown voltage for the punch-through diode is reduced due to the truncation of the electric field at the N^+ end region. The breakdown voltage becomes smaller as the thickness of the drift region is reduced. From the point of view of designing the drift region for a P-i-N rectifier, it is possible to obtain a breakdown voltage of 1000 V with a drift region thickness of about 50 μm. In contrast, a drift region thickness of 80 μm would be required in the non-punch-through case. This reduced drift region thickness with the punch-through design is beneficial for not only reducing the on-state voltage drop but for reducding the stored charge and, consequently, the reverse recovery power loss as discussed later in the book in Chapter 5.

A similar analysis for the breakdown voltages can be performed for punch-through diodes fabricated from 4H-SiC, as shown in Fig. 3.9, with various

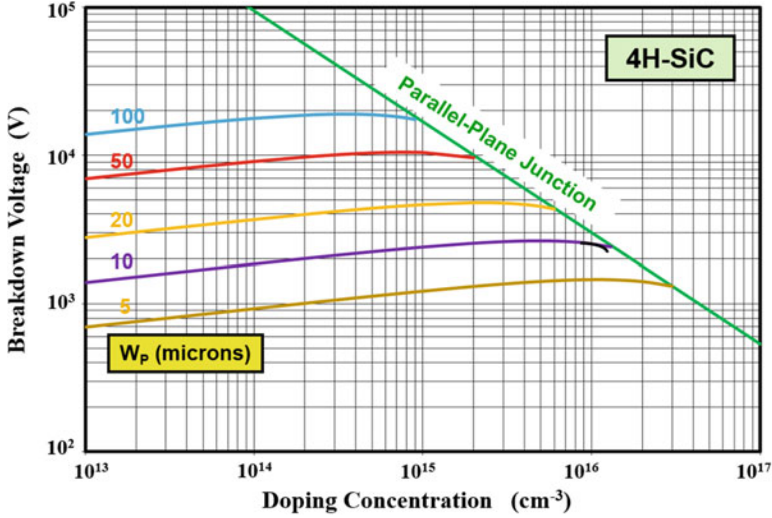

Fig. 3.9 Breakdown voltages for the 4H-SiC P-i-N diodes with punch-through design

thicknesses for the drift region. In performing these calculations, the change in the critical electric field with doping concentration, as described by Eq. (3.23), must be taken into account. In comparison with silicon punch-through diodes, a much higher (~10×) doping concentration can be used in the drift region for 4H-SiC to achieve the punch-through design with a given thickness for the drift region. From the point of view of designing the drift region for a P-i-N rectifier, it is possible to obtain a breakdown voltage of 10,000 V with a drift region thickness of about 50 μm in 4H-SiC. In contrast, a drift region thickness of 80 μm would be required in the non-punch-through case. This reduced drift region thickness with the punch-through design is beneficial for reducing the on-state voltage drop. However, the minority carrier lifetime in 4H-SiC has been found to be low resulting in poor conductivity modulation of the drift region. It is therefore advisable to maintain a high doping concentration in the drift region for P-i-N rectifiers fabricated from 4H-SiC.

The maximum electric field for the punch-through case is actually slightly larger than for the non-punch-through case because of the shorter avalanche path. The breakdown voltage, shown in Fig. 3.8 and 3.9, then becomes nearly independent of the doping concentration for the punch-through case as the doping concentration is reduced.

3.5 Linearly Graded Junction Diode

Power devices fabricated using junctions with high surface doping concentration and shallow thickness tend to behave like the abrupt junction diodes that were discussed in the previous sections. Power devices, such as thyristors, that are designed to

support very high voltages (above 2000 V) rely upon junctions with low surface concentration and large depth to enhance the blocking voltage capability. In addition, power devices with low (<50 V) blocking voltages, such as low-voltage power MOSFETs, require drift regions with relatively high doping concentrations that are comparable to the doping level on the diffused side of the junction. A significant fraction of the reverse bias voltage is supported within the diffused side of the junction in this case as well.

These types of junctions can be analyzed by assuming a linearly graded doping profile in the vicinity of the junction. A typical doping profile for a diffused junction diode is illustrated in Fig. 3.10. For diffused junctions, it is customary to plot the profile with the doping concentration displayed using a logarithmic scale as shown in the upper part of the figure. Due to the compensation of the N-region by the P-type dopant in the vicinity of the junction, the profile has a linear net doping distribution as illustrated in the lower portion of the figure. The diffused junction can therefore be treated as a combination of a linearly graded junction and a uniformly doped junction.

If the linear doping grading is sufficiently steep, the maximum electric field at the junction can reach the critical electric field with the depletion region confined to this portion of the doping profile. The linearly graded junction is illustrated in Fig. 3.11 together with the electric field and potential distributions. Note that the depletion region extends to both sides of the metallurgical junction by a distance *W*. With a

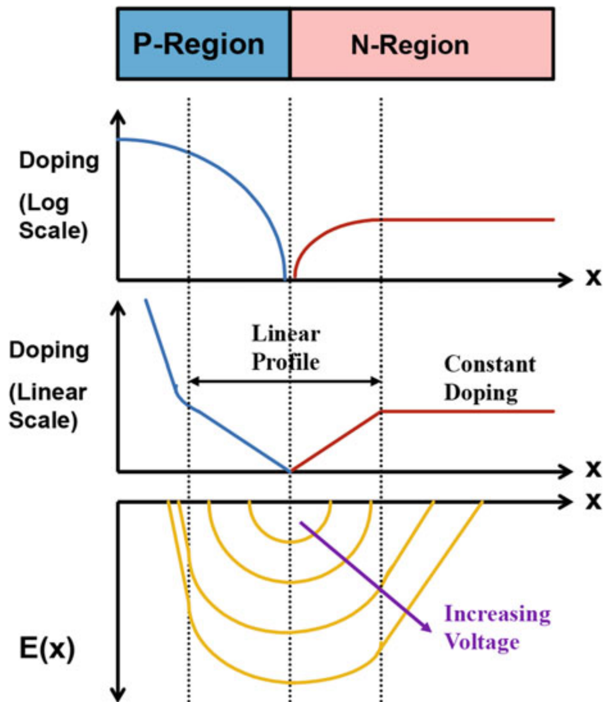

Fig. 3.10 The diffused junction diode

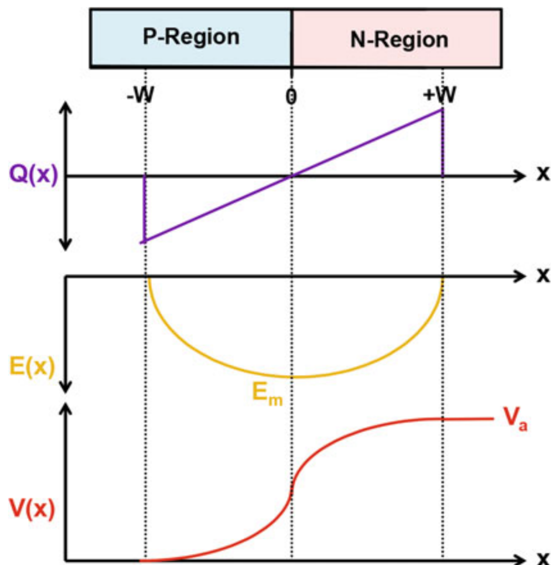

Fig. 3.11 The linearly graded junction diode

positive voltage applied to the N-region, the junction becomes reverse biased with a net negative charge on the P-side due to the ionized acceptors having a greater concentration than the donors while a net positive charge develops on the N-side due to the ionized donors having a greater concentration than the acceptors. The concentration of the net charge varies linearly with distance with a grade constant G.

The breakdown voltage of this linearly graded junction can be analyzed by using the following charge distribution profile in Poisson's equation:

$$Q(x) = qGx \tag{3.29}$$

Applying this charge distribution to Poisson's equation gives:

$$\frac{d^2V}{dx} = -\frac{dE}{dx} = -\frac{Q(x)}{\varepsilon_S} = \frac{-qGx}{\varepsilon_S} \tag{3.30}$$

Integration of this equation with the boundary condition that the electric field must be zero at the edge of the depletion region ($x = W$) provides the electric field distribution:

$$E(x) = \frac{qG}{2\varepsilon_S}\left(x^2 - W^2\right) \tag{3.31}$$

The electric field varies parabolically with distance with its maximum value at the junction given by:

$$E_m = \frac{qGW^2}{2\varepsilon_S} \tag{3.32}$$

Integration of the electric field distribution through the depletion region with the boundary conditions that the potential is zero at $x = -W$ on the P-side of the junction yields:

$$V(x) = \frac{qG}{\varepsilon_S}\left(\frac{W^3}{3} + \frac{W^2 x}{2} - \frac{x^3}{6}\right) \tag{3.33}$$

This voltage distribution is shown at the bottom of Fig. 3.11. The depletion layer width (W) on both sides of the junction can be obtained by using the boundary condition that the voltage on the N-side of the junction is equal to the applied bias (V_a):

$$W = \left(\frac{3\varepsilon_S V_a}{qG}\right)^{1/3} \tag{3.34}$$

In the case of devices, such as power MOSFETs, the extension of the depletion layer on the diffused side of the junction can lead to reach-thorough breakdown at well below the avalanche breakdown voltage. The depletion width calculated by using Eq. (3.34), based upon approximation of the diffused junction by a linearly graded junction, provides an analytical approach to designing the width of the P-base region.

A closed form analytical solution for the breakdown voltage of the linearly graded junction can be obtained by determination of the voltage at which the impact ionization integral becomes equal to unity. Using the ionization integral given by Eq. (3.17) with Fulop's approximation for the impact ionization coefficients and the electric field distribution given by Eq. (3.31):

$$\int_{-W}^{W} 1.8 \times 10^{-35}\left[\frac{qG}{2\varepsilon_S}\left(x^2 - W^2\right)\right]^7 dx = 1 \tag{3.35}$$

The solution for this equation provides the depletion width at the point of breakdown for the linearly graded junction:

$$W_{CL} = 9.1 \times 10^5 . G^{-7/15} \tag{3.36}$$

Using this depletion width in Eq. (3.34), the breakdown voltage for the linearly graded junction is found to be given by:

$$BV_L = 9.2 \times 10^9 . G^{-2/5} \tag{3.37}$$

As illustrated by the electric field distribution in Fig. 3.10, the diffused junction diode usually behaves as a combination of a linearly graded junction and an abrupt junction with uniform doping on the lightly doped side. The extension of the depletion region into the diffused side of the junction enhances the breakdown voltage to above that derived earlier for the abrupt parallel-plane junction because

of the additional voltage that is supported on the diffused side of the junction. This can be taken advantage of during the design of low (<30 V) voltage power MOSFETs.

3.6 Edge Terminations

All semiconductor devices have a finite size, which is achieved by sawing through the wafers to produce the chips that go into packages. The sawing of wafers, performed by using diamond coated blades, produces severe damage to the crystal. In the case of power devices, if the sawing is performed through the junction that must support a high voltage, the crystal damage creates a high leakage current that degrades the breakdown voltage and its stability with respect to time. This problem can be addressed by using special junction terminations around the edges of the power devices so that the depletion regions of the high-voltage junctions do not intersect with the saw lanes where the damage is located. Another approach that can be used to control and preserve a high breakdown voltage is by shaping the surface of the edges of the device. The earliest method for shaping the edges was by mesa etching. Subsequently, the beveling of the edges of wafers was found to be very effective in preserving the breakdown voltage of high-voltage power rectifiers and thyristors. With the widespread availability of ion implantation for the fabrication of power devices in the 1980s, the use of a lightly doped zone at the edges of junctions has been found to be effective in achieving high breakdown voltages. These methods for enhancing the breakdown voltage of power devices are discussed in this section.

3.6.1 Planar Junction Termination

A cornerstone of modern semiconductor devices is the planar junction formed by the diffusion of impurities through a window in a silicon dioxide mask grown on the silicon surface. Consider a rectangular window etched in a silicon dioxide masking layer on an N-type silicon substrate as illustrated in the upper part of Fig. 3.12. The dopant can be diffused into the silicon surface exposed within the window by dopants introduced via the vapor phase or by low energy ion implantation. It is customary to thermally drive the dopant atoms into the silicon at elevated temperatures in order to produce junction depths appropriate for power devices. During this drive-in process, the dopants migrate vertically downward within the diffusion window to produce a parallel-plane junction. However, at the edges of diffusion window, the dopants migrate laterally under the silicon dioxide while being driven downward. If the lateral diffusion is assumed to be equal to the junction depth, this process produces a cylindrical shaped junction at the edges of the diffusion window as illustrated at the bottom of the figure. The breakdown voltage of the planar junction is reduced by the presence of this junction curvature [9].

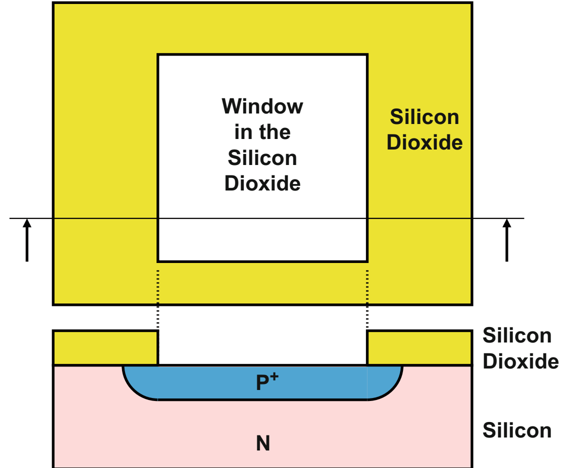

Fig. 3.12 The planar junction obtained by diffusion through a window in a silicon dioxide mask

A sharp point is formed at the corners of the rectangular diffusion window. The dopants are driven in three dimensions away from this corner producing a junction which is one-eighth of a spherical surface. An even greater electric field enhancement occurs due to the presence of these spherical junctions at the four corners of the rectangular window. The breakdown voltage at these locations is consequently lower than that at the edges of the window where the cylindrical junctions are located. Lateral diffusion in silicon under a silicon dioxide mask has been found to be 85% of the vertical depth. These junctions can be approximated as either cylindrical or spherical junctions in order to derive analytical solutions to the breakdown voltage.

Cylindrical Junction

A cross section of the cylindrical junction is shown in Fig. 3.13 with junction depth of r_J. If the P^+ diffused side of the junction is assumed to have a very high doping concentration when compared with the N-type substrate, the depletion layer will extend only on the N-side as shown in the figure to a depth r_D. The analysis of the breakdown of this structure has been performed by numerical simulations [10]. The breakdown voltage for the cylindrical junction can also be analytically obtained by solving Poisson's equation in cylindrical coordinates [11]:

$$\frac{1}{r}\frac{d}{dr}\left(r\frac{dV}{dr}\right) = -\frac{1}{r}\frac{d}{dr}(r.E) = -\frac{Q(r)}{\varepsilon_S} = -\frac{q.N_D}{\varepsilon_S} \tag{3.38}$$

where the potential $V(r)$ and electric field $E(r)$ are defined along the radius vector r extending into the depletion region as shown in Fig. 3.13. Integration of this equation with the boundary condition that the electric field must be zero at the

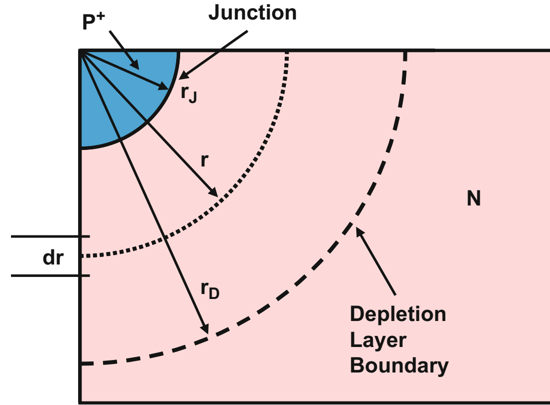

Fig. 3.13 The cylindrical junction

depletion region boundary (r_D) in the N-type region provides the electric field distribution:

$$E(r) = \frac{qN_D}{2\varepsilon_S}\left(\frac{r^2 - r_D^2}{r}\right) \tag{3.39}$$

As in the case of the parallel-plane junction, the maximum value for the electric field occurs at the metallurgical junction located at $r = r_J$:

$$E_{m,CYL}(r_J) = \frac{qN_D}{2\varepsilon_S}\left(\frac{r_J^2 - r_D^2}{r_J}\right) \tag{3.40}$$

The maximum electric field generated in the cylindrical junction is significantly larger than that observed in the parallel-plane case. This can be demonstrated by considering the case of a cylindrical junction whose radius of curvature (r_J) is small when compared with the depletion width and consequently the radius r_D. Since r_J is much smaller than r_D in this case, the maximum electric field is given by:

$$E_{m,CYL}(r_J) = -\frac{qN_D r_D^2}{2\varepsilon_S r_J} \tag{3.41}$$

The maximum electric field for the parallel-plane junction is given by Eq. (3.12) with $x = 0$:

$$E_{m,PP} = -\frac{qN_D W_D}{\varepsilon_S} \tag{3.42}$$

If the depletion widths for the two cases are assumed to be approximately equal at the same reverse bias voltage (i.e., $r_D = W_D$), then the enhancement of the electric field at the cylindrical junction can be obtained by taking the ratio of the maximum electric field for the two cases:

$$\frac{E_{\mathrm{m,CYL}}}{E_{\mathrm{m,PP}}} = \frac{r_{\mathrm{D}}}{2r_{\mathrm{J}}} \tag{3.43}$$

From this equation, it can be concluded that, for shallow junctions with small radii of curvature, the maximum electric field is significantly larger than for the parallel-plane case. For example, if the junction depth is 1 μm and the depletion region has a thickness of 30 μm, the maximum electric field at the cylindrical junction will be 15 times larger than that for the parallel-plane case. Since impact ionization is a very strong function of the electric field, avalanche breakdown will occur at a lower voltage for the cylindrical junction than for a parallel-plane junction with the same doping concentration on the lightly doped side.

The potential distribution for the cylindrical junction, obtained by integration of the electric field distribution, is given by:

$$V(r) = \frac{qN_{\mathrm{D}}}{2\varepsilon_{\mathrm{S}}}\left[\left(\frac{r^2 - r_{\mathrm{J}}^2}{2}\right) + r_{\mathrm{D}}^2 \ln\left(\frac{r}{r_{\mathrm{J}}}\right)\right] \tag{3.44}$$

The width of the depletion layer for the cylindrical junction can be obtained by using the boundary conditions for the voltage, namely, the voltage being equal to zero on the highly doped side and V_{a} in the lightly doped side. The breakdown voltage for the cylindrical junction can be obtained by performing the ionization integral using the electric field distribution given by Eq. (3.39). In order to obtain a closed form solution for the ionization integral, it is convenient to make the approximation that the electric field varies inversely with distance from the junction:

$$E(r) = -\frac{qN_{\mathrm{D}}}{2\varepsilon_{\mathrm{S}}}\frac{r_{\mathrm{D}}^2}{r} = -\frac{K_{\mathrm{C}}}{r} \tag{3.45}$$

The electric field distribution obtained by using this hyperbolic approximation is compared with that given by Eq. (3.39) in Fig. 3.14 for the case of $r_{\mathrm{J}} = 0.1\ r_{\mathrm{D}}$. The hyperbolic approximation provides a good fit to the exact case in the vicinity of the junction where the electric field is large. Since the impact ionization coefficients are a very strong function of the electric field, the approximation is satisfactory for the evaluation of the ionization integral. It is worth pointing out that the hyperbolic approximation implies that the electric field distribution extends to an infinite distance from the junction. Consequently, the ionization integral must also be performed to infinity when using the hyperbolic approximation for the electric field.

Evaluation of the ionization integral using the hyperbolic variation of the electric field together with Baliga's law for the ionization coefficient for silicon yields a solution for the breakdown condition for the cylindrical junction:

$$K_{\mathrm{C}} = \left(\frac{6\,r_{\mathrm{J}}^6}{3.507 \times 10^{-35}}\right)^{1/7} = \frac{qN_{\mathrm{D}}r_{\mathrm{D}}^2}{2\varepsilon_{\mathrm{S}}} \tag{3.46}$$

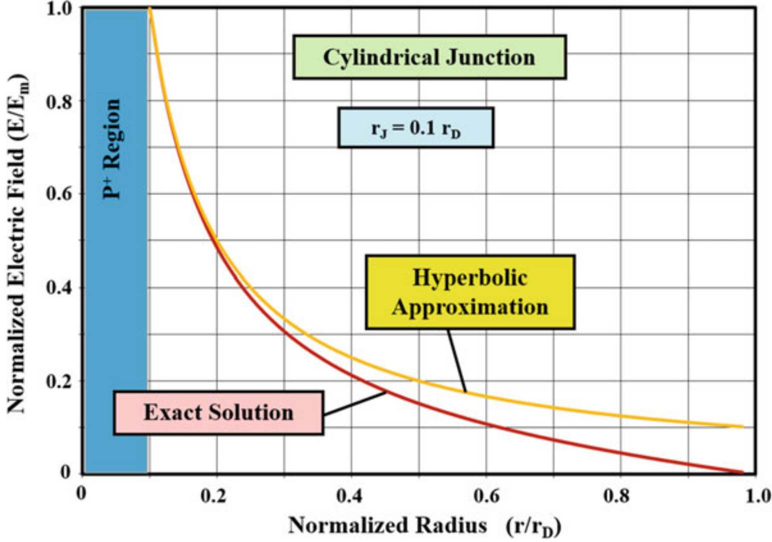

Fig. 3.14 Comparison of the electric field distribution for the hyperbolic approximation with the exact case for a cylindrical junction

By combining this condition for breakdown with Eq. (3.41) for the maximum electric field, the critical electric field for breakdown at the cylindrical junction is obtained:

$$E_{\mathrm{C,CYL}} = \left(\frac{1.711 \times 10^{35}}{r_{\mathrm{J}}}\right)^{1/7} \tag{3.47}$$

The critical electric field for breakdown in the case of cylindrical junctions can be compared with the critical electric field for the parallel-plane junction by taking their ratio:

$$\frac{E_{\mathrm{C,CYL}}}{E_{\mathrm{C,PP}}} = \left(\frac{3\,W_{\mathrm{PP}}}{4\,r_{\mathrm{J}}}\right)^{1/7} \tag{3.48}$$

In deriving this relationship, the critical electric field ($E_{\mathrm{C,PP}}$) for the parallel-plane case was related to the depletion width (W_{PP}) by using Eqs. (3.19) and (3.22). Since the radius of curvature of the junction is assumed to be small compared with the depletion layer thickness, the above relationship indicates that the critical electric field for breakdown in the cylindrical junction is larger than that for the parallel-plane junction. This difference is associated with the high electric field being located over a shorter distance in the case of the cylindrical junction when compared with the parallel-plane junction.

The breakdown voltage for the cylindrical junction can be obtained by using $r = r_D$ in Eq. (3.44) with the value for r_D defined by the breakdown condition as governed by Eq. (3.46). In order to generalize the solution to represent a wide variety of junctions with different doping concentrations on the lightly doped side, it is convenient to normalize the breakdown voltage of the cylindrical junction to that for the parallel-plane case. In order to obtain this generalized solution, it is also convenient to normalize the radius of curvature of the junction to the depletion layer thickness at breakdown for the parallel-plane junction. This methodology provides the normalized breakdown voltage for the cylindrical junction:

$$\frac{BV_{CYL}}{BV_{PP}} = \frac{1}{2}\left[\left(\frac{r_J}{W_{PP}}\right)^2 + 2\left(\frac{r_J}{W_{PP}}\right)^{6/7}\right] . \ln\left[1 + 2\left(\frac{W_{PP}}{r_J}\right)^{8/7}\right] - \left(\frac{r_J}{W_{PP}}\right)^{6/7} \tag{3.49}$$

It is worth pointing out that this relationship was derived under the assumption that the radius of curvature of the junction is small when compared with the depletion layer thickness (i.e., $r_J/W_{PP} << 1$). Since power devices are usually fabricated with shallow junctions when compared with the large depletion layer widths required to support high voltages, the above equation is usually valid for their analysis.

The normalized breakdown voltage for cylindrical junctions as predicted by the above equation is plotted in Fig. 3.15 as a function of the normalized radius of curvature. This graph is valid for junctions fabricated from any doping concentration on the lightly doped side as long as the radius of curvature is small when compared with the depletion layer width at breakdown for the parallel-plane junction with the

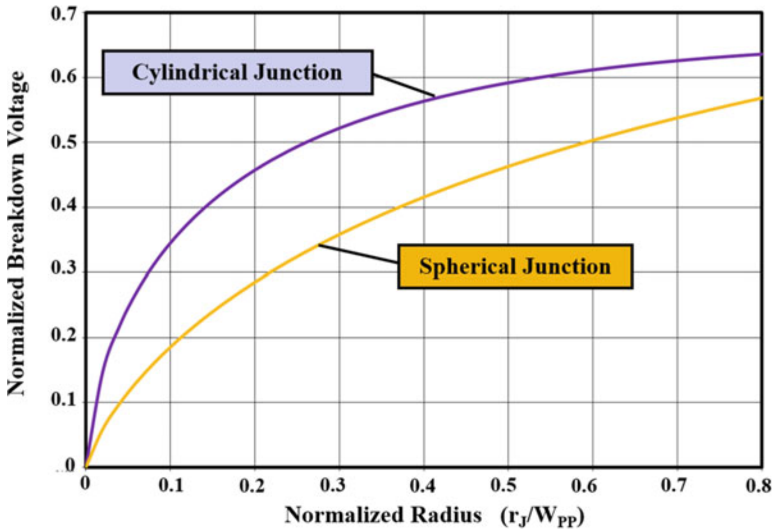

Fig. 3.15 Breakdown voltages of cylindrical and spherical junctions normalized to the parallel-plane case

same doping concentration on the lightly doped side. It can be seen that the breakdown voltage for the cylindrical junction increases when the radius of curvature (or junction depth) is increased. Shallower junction can be used for power devices with lower breakdown voltages due to the relatively high doping concentration and small depletion layer widths in the drift region. Power devices with high breakdown voltages require large junction depths to reduce the degradation of the breakdown voltage due to junction curvature. As an example, if a junction depth of 3 μm is used with a background doping concentration of 1×10^{15} cm^{-3} corresponding to a depletion layer width of 18 μm, the normalized breakdown voltage is 42.7% of the breakdown voltage for the parallel-plane case. However, if the doping concentration of the drift region is reduced to 4×10^{14} cm^{-3} corresponding to a depletion layer width of 40 μm, the normalized breakdown voltage is reduced to only 30% of the breakdown voltage for the parallel-plane case. In practice, it is impractical to obtain a normalized radius of curvature of more than 0.4 making it difficult to raise the normalized breakdown voltage for the cylindrical junction to above 50% of the parallel-plane case. It is therefore common practice to incorporate floating field rings and field plates to enhance the breakdown voltage of cylindrical junctions as discussed later in the chapter.

Simulation Example

The results of two-dimensional numerical simulations are provided in this section for the case of a drift region with doping concentration of 3.8×10^{14} cm^{-3} to gain further insight into the physics of operation for the cylindrical junction. The simulations were performed by using impact ionization coefficients reported in the literature for silicon [12]. At this doping concentration, the parallel-plane breakdown voltage was found to be 520 V with a depletion region thickness of 41 μm for the case of a P^+ region with a surface doping concentration of 1×10^{20} cm^{-3} and depth of 5 μm. The breakdown voltage obtained with the simulations matches that predicted by the analytical formulation in Eq. (3.18) based up on Baliga's power law for the impact ionization coefficient for silicon. The electric field at the junction was found to be 2.35×10^5 V/cm at breakdown. This field matches the critical electric field for breakdown predicted by Eq. (3.22) based up on Baliga's power law for the impact ionization coefficient for silicon.

The breakdown voltages of planar junctions with cylindrical curvature were obtained by performing simulations with various junction depths ranging from 2 to 20 μm. The breakdown voltages obtained with the two-dimensional numerical simulations for the various junction depths were normalized to the breakdown voltage of the parallel-plane junction as determined by the simulations. The normalized breakdown voltage for these cylindrical junctions is plotted in Fig. 3.16 as a function of the normalized radius of curvature together with the analytically derived curve previously shown in Fig. 3.15. A good agreement between the results of the simulations and the analytical formulation is observed at small junction depths confirming that the analytical model provides a reasonable approach for the analysis of the breakdown voltage for cylindrical junctions. However, the analytical model

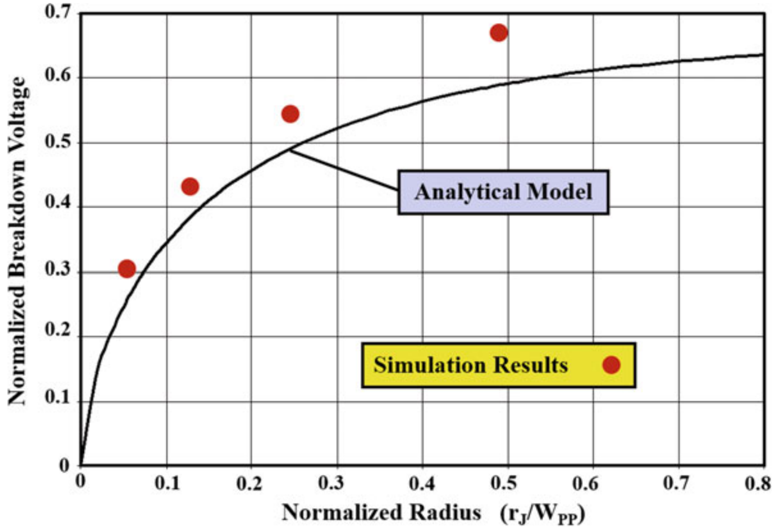

Fig. 3.16 Breakdown voltages of cylindrical junctions: comparison of simulated results with analytical model

underestimates the breakdown voltage by more than 10% when the normalized junction depth is larger than 0.4.

A three-dimensional view of the electric field at the cylindrical junction is shown in Fig. 3.17 for the case of a junction depth of 5 μm at a reverse bias of 200 V. It can be seen that there is an enhancement in the electric field at the corner of the junction with much larger electric fields in this location when compared with the middle of the junction. The degree of enhancement of the electric field depends upon the radius of curvature of the junction. This is illustrated in Fig. 3.18 by comparing the electric field profile at various reverse bias voltages for junctions with different depths. It can be observed that a larger electric field develops at the cylindrical junction at the same magnitude for the reverse bias voltage (see arrows at $V_R = 150$ V for the three cases) when its junction depth is smaller. This is responsible for a reduction in the breakdown voltage.

Spherical Junction

It is common practice to fabricate devices in integrated circuits by using rectangular windows, as illustrated in Fig. 3.12, because this simplifies the layout of the chip. As already discussed, a spherical junction is formed at each of the four corners of the rectangular diffusion window. A cross-sectional view of this spherical junction is identical to that illustrated in Fig. 3.13 for the cylindrical junction. However, the electric field is enhanced even further than for the cylindrical junction because the field lines approach a point in three dimensions for the spherical junction, while they

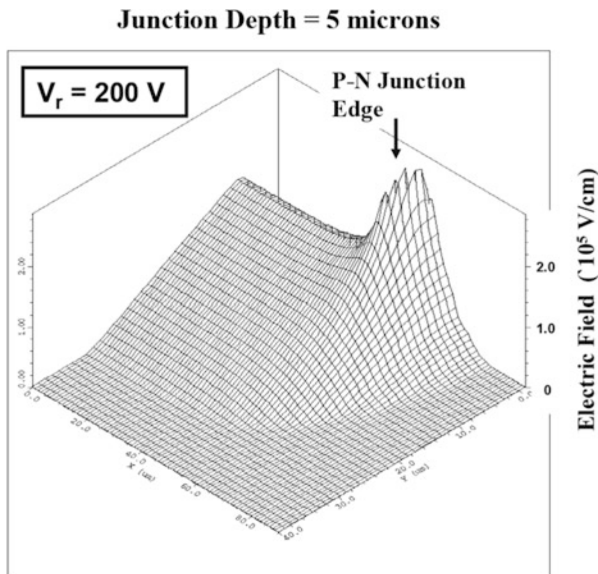

Fig. 3.17 Electric field distribution in a cylindrical junction

approach a line from two dimensions for the cylindrical junction. This difference in behavior can be analyzed by performing the solution for Poisson's equation [11] in spherical coordinates:

$$\frac{1}{r^2}\frac{d}{dr}\left(r^2\frac{dV}{dr}\right) = -\frac{1}{r^2}\frac{d}{dr}\left(r^2E\right) = -\frac{Q(r)}{\varepsilon_S} = -\frac{qN_D}{\varepsilon_S} \tag{3.50}$$

where the potential $V(r)$ and electric field $E(r)$ are defined along the radius vector r extending into the depletion region as shown in Fig. 3.13. Integration of this equation with the boundary condition that the electric field must be zero at the depletion region boundary (r_D) in the N-type region provides the electric field distribution:

$$E(r) = \frac{qN_D}{3\varepsilon_S}\left(\frac{r^3 - r_D^3}{r^2}\right) \tag{3.51}$$

The maximum value for the electric field for the spherical junction also occurs at the metallurgical junction located at $r = r_J$:

$$E_{m,SP}(r_J) = \frac{qN_D}{3\varepsilon_S}\left(\frac{r_J^3 - r_D^3}{r_J^2}\right) \tag{3.52}$$

The maximum electric field generated in the spherical junction is not only significantly larger than that observed in the parallel-plane case but exceeds that generated in the cylindrical junction. This can be demonstrated by considering the case of a

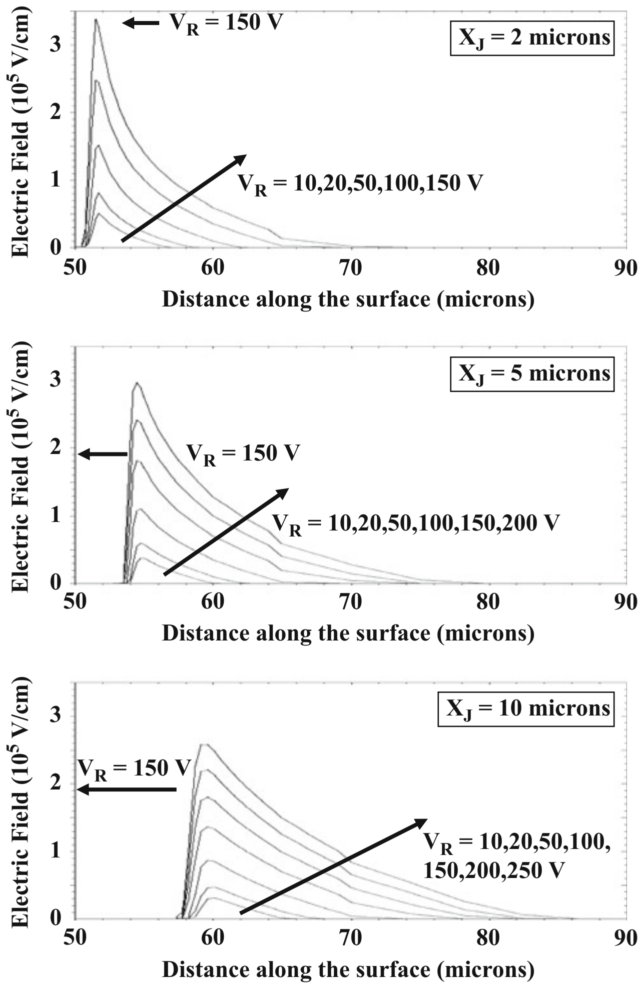

Fig. 3.18 Electric field profiles in cylindrical junctions with various junction depths

spherical junction whose radius of curvature (r_J) is small when compared with the depletion width and consequently the radius r_D. Since r_J is much smaller than r_D in this case, the maximum electric field is given by:

$$E_{m,SP}(r_J) = -\frac{qN_D r_D^3}{3\varepsilon_S r_J^2} \tag{3.53}$$

If the depletion widths for the spherical and cylindrical cases are assumed to be approximately equal at the same reverse bias voltage (i.e., $r_D = W_D$), then the enhancement of the electric field at the spherical junction over that at the cylindrical

junction can be obtained by taking the ratio of the maximum electric field for the two cases:

$$\frac{E_{\mathrm{m,SP}}}{E_{\mathrm{m,CYL}}} = \frac{2r_{\mathrm{D}}}{3r_{\mathrm{J}}} \tag{3.54}$$

From this equation, it can be concluded that, for shallow junctions with small radii of curvature, the maximum electric field generated at the sharp corners of diffusion windows is significantly larger than along the sides of the window. For example, if the junction depth is 1 μm and the depletion region has a thickness of 30 μm, the maximum electric field at the spherical junction will be 20 times larger than that at the cylindrical junction. Since impact ionization is a very strong function of the electric field, avalanche breakdown will occur at the corners of the rectangular diffusion window at a lower voltage than at the edges or middle of the diffused region.

The potential distribution for the spherical junction, obtained by integration of the electric field distribution, is given by:

$$V(r) = \frac{qN_{\mathrm{D}}}{3\varepsilon_{\mathrm{S}}}\left[\left(\frac{r^2 - r_{\mathrm{J}}^2}{2}\right) + r_D^3\left(\frac{1}{r} - \frac{1}{r_{\mathrm{J}}}\right)\right] \tag{3.55}$$

The width of the depletion layer for the spherical junction can be obtained by using the boundary conditions for the voltage, namely, the voltage being equal to zero on the highly doped side and V_{a} in the lightly doped side. The breakdown voltage for the spherical junction can be obtained by performing the ionization integral using the electric field distribution given by Eq. (3.51). In order to obtain a closed form solution for the ionization integral, it is convenient to make the approximation that the electric field varies inversely as the square of the distance from the junction:

$$E(r) = -\frac{qN_{\mathrm{D}}}{3\varepsilon_{\mathrm{S}}}\frac{r_{\mathrm{D}}^3}{r^2} = -\frac{K_{\mathrm{S}}}{r^2} \tag{3.56}$$

The electric field distribution obtained by using this inverse square approximation is compared with that given by Eq. (3.51) in Fig. 3.16 for the case of $r_{\mathrm{J}} = 0.1\ r_{\mathrm{D}}$. The inverse square approximation provides a very good fit to the exact case especially in the vicinity of the junction where the electric field is large. Since the impact ionization coefficients are a very strong function of the electric field, the approximation is satisfactory for the evaluation of the ionization integral. It is worth pointing out that this approximation implies that the electric field distribution extends to an infinite distance from the junction. Consequently, the ionization integral must also be performed to infinity when using the inverse square approximation for the electric field (Fig. 3.19).

Evaluation of the ionization integral using the inverse square variation of the electric field together with Baliga's law for the ionization coefficient yields a solution for the breakdown condition for the cylindrical junction:

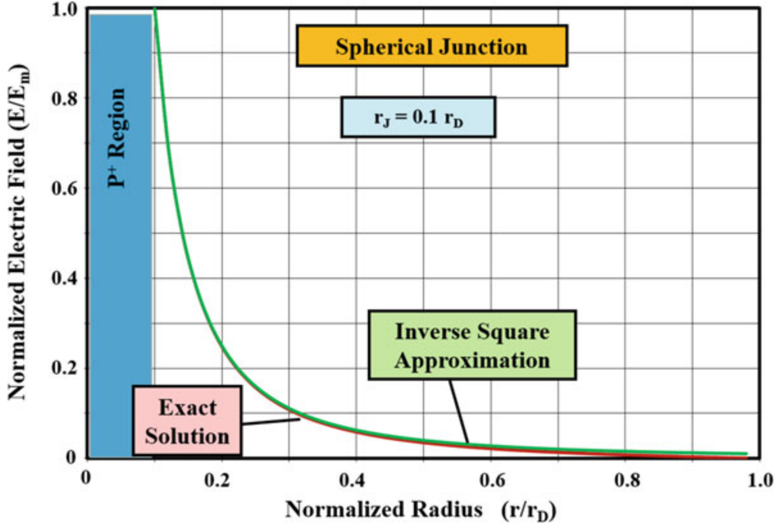

Fig. 3.19 Comparison of the electric field distribution for the inverse square approximation with the exact case for a spherical junction

$$K_{SP} = \left(\frac{13 r_J^{13}}{3.507 \times 10^{-35}}\right)^{1/7} = \frac{q N_D r_D^3}{3 \varepsilon_S} \quad (3.57)$$

By combining this condition for breakdown with Eq. (3.53) for the maximum electric field, the critical electric field for breakdown at the spherical junction is obtained:

$$E_{C,SP} = \left(\frac{3.71 \times 10^{35}}{r_J}\right)^{1/7} \quad (3.58)$$

The critical electric field for breakdown in the case of cylindrical junctions can be compared with the critical electric field for the parallel-plane junction by taking their ratio:

$$\frac{E_{C,SP}}{E_{C,PP}} = \left(\frac{13 W_{PP}}{8 r_J}\right)^{1/7} \quad (3.59)$$

In deriving this relationship, the critical electric field ($E_{C,PP}$) for the parallel-plane case was related to the depletion width (W_{PP}) by using Eqs. (3.19) and (3.22). Since the radius of curvature of the junction is assumed to be small compared with the depletion layer thickness, the above relationship indicates that the critical electric field for breakdown in the spherical junction is larger than that for the parallel-plane junction. This difference is associated with the high electric field being located over a

shorter distance in the case of the spherical junction when compared with the parallel-plane junction.

The breakdown voltage for the spherical junction can be obtained by using $r = r_D$ in Eq. (3.55) with the value for r_D defined by the breakdown condition as governed by Eq. (3.57). In order to generalize the solution to represent a wide variety of junctions with different doping concentrations on the lightly doped side, it is convenient to normalize the breakdown voltage of the spherical junction to that for the parallel-plane case. In order to obtain this generalized solution, it is also convenient to normalize the radius of curvature of the junction to the depletion layer thickness at breakdown for the parallel-plane junction. This methodology provides the normalized breakdown voltage for the spherical junction:

$$\frac{BV_{SP}}{BV_{PP}} = \left(\frac{r_J}{W_{PP}}\right)^2 + 2.14\left(\frac{r_J}{W_{PP}}\right)^{6/7} - \left[\left(\frac{r_J}{W_{PP}}\right)^3 + 3\left(\frac{r_J}{W_{PP}}\right)^{13/7}\right]^{2/3} \tag{3.60}$$

It is worth pointing out that this relationship was derived under the assumption that the radius of curvature of the junction is small when compared with the depletion layer thickness (i.e., $r_J/W_{PP} < < 1$). Since power devices are usually fabricated with shallow junctions when compared with the large depletion layer widths required to support high voltages, the above equation is usually valid for their analysis.

The normalized breakdown voltage for spherical junctions as predicted by the above equation is also plotted in Fig. 3.15 as a function of the normalized radius of curvature. This graph is valid for junctions fabricated from any doping concentration on the lightly doped side as long as the radius of curvature is small when compared with the depletion layer width at breakdown for the parallel-plane junction with the same doping concentration on the lightly doped side. It can be seen that the breakdown voltage for the spherical junction increases when the radius of curvature (or junction depth) is increased.

The breakdown voltage at the spherical junctions formed at the corners of the rectangular diffusion window is substantially lower than the breakdown voltage at the cylindrical junctions formed at the straight edges of the window. For instance, at a normalized radius of curvature of 0.2, the breakdown voltage is reduced from 46% to 28% of the parallel-plane value. This is detrimental to achieving low on-state voltage drops in power devices because the doping concentration must be reduced and thickness of the drift region must be increased to achieve the desired breakdown voltage in the presence of the spherical junction curvature. This problem can be overcome by rounding the corners of the diffusion window. It is a common practice to design the windows of high-voltage power devices with the corners rounded with a radius that is at least twice the thickness of the depletion region (W_{PP}) for the parallel-plane junction at breakdown for the drift region.

3.6.2 Planar Junction with Floating Field Ring

An elegant method for improving the breakdown voltage of planar junctions is by surrounding the diffusion window with a floating field ring [13]. This can be implemented by opening a diffusion window for the floating field ring simultaneously with the main junction with no additional process steps. A top view of the structure is shown in Fig. 3.20 together with a cross section taken at the red line with the red arrows. Note that there is no metal contact made to the floating field ring allowing it to attain a potential intermediate to the voltage applied to the cathode. Although the depth of the floating field ring could be greater or smaller than the main junction, in practice the floating field ring is invariably fabricated at the same time as the main junction giving it the same depth. The analysis in this section will therefore be confined to this case.

In order for the floating field ring to perturb the electric field at the main junction, it must be located within the depletion width of the main junction. The optimum location of the floating field ring has been determined by numerical simulations [14]. If the spacing of the floating ring is too close to the main junction, its potential becomes close to that of the main junction and the breakdown voltage is not substantially improved because a high electric field develops at the floating field

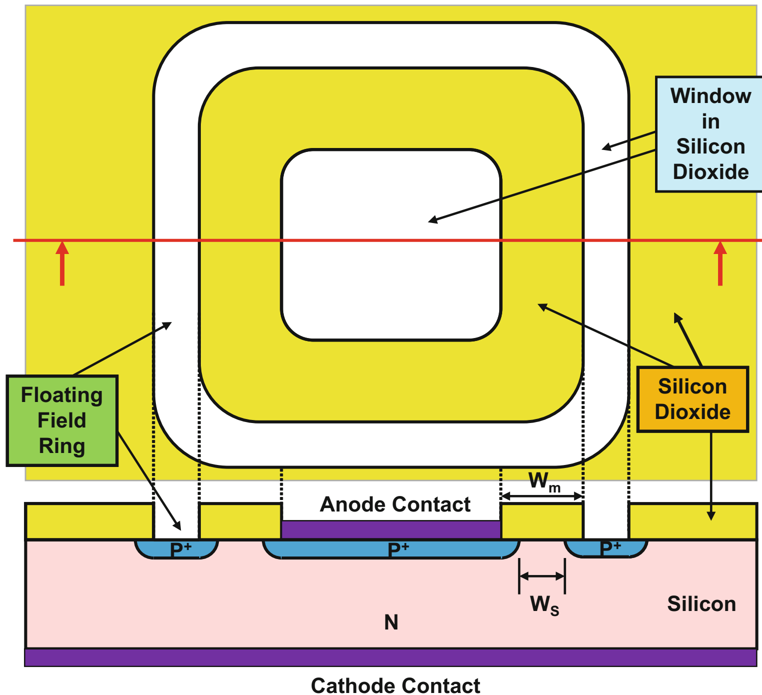

Fig. 3.20 The planar junction with floating field ring

ring. On the other hand, if the floating field ring is placed too far from the main junction, it has minimal effect on the electric field at the main junction resulting in insubstantial improvement in the breakdown voltage. It is necessary to place the floating field ring at an optimal spacing in order to provide an improvement in the breakdown voltage. It is worth pointing out that the spacing on the mask for the design of the floating field ring termination must take into account the lateral diffusion of the junctions. Once the optimum spacing of W_S is obtained, the spacing on the mask is given by:

$$W_m = W_S + 2x_J \tag{3.61}$$

The potential assumed by the floating field ring can be analytically determined under the assumption that the presence of the floating field ring does not perturb the extension of the depletion region from the main junction. If the floating ring is assumed to have a small width then its potential can be assumed to equal to the potential within the depletion region at a distance W_S from the junction. Using the potential distribution for the parallel-plane junction given by Eq. (3.13) with $x = W_S$ and a depletion width of W_D:

$$V_{FFR} = \frac{qN_D}{\varepsilon_S}\left(W_D W_S - \frac{W_S^2}{2}\right) \tag{3.62}$$

Replacing W_D by using Eq. (3.15):

$$V_{FFR} = \sqrt{\frac{2qN_D W_S^2 V_a}{\varepsilon_S}} - \frac{qN_D W_S^2}{2\varepsilon_S} \tag{3.63}$$

This equation indicates that the potential of the floating field ring will increase as the square root of the applied bias to the cathode. It is worth pointing out that this equation is valid only when the depletion layer width of the main junction exceeds the field ring spacing. When the applied reverse bias is insufficient to allow the depletion layer from the main junction to overlap the floating field ring, the potential of the floating field ring is equal to the reverse bias applied to the cathode.

The potential of the floating field ring calculated by using the above formula is shown in Fig. 3.21 for various examples of the field ring spacing together with the case of a very large field ring spacing where the field ring potential to equal to the applied bias to the cathode. For the smallest spacing of 3 μm, the potential at the field ring increases in proportion to the applied bias up to about 10 V and then increases at a more gradual rate after the depletion layer from the main junction extends to the floating field ring. When the field ring spacing is increased to 5, 10, and 15 μm, this transition occurs at a larger applied bias of about 20, 40, and 100 V, respectively. This has a strong influence on the electric field at the edges of the main junction and floating field ring junction.

As discussed earlier, the floating field ring must be located at an optimal position in order to maximize the breakdown voltage. With an optimum spacing (W_S), the

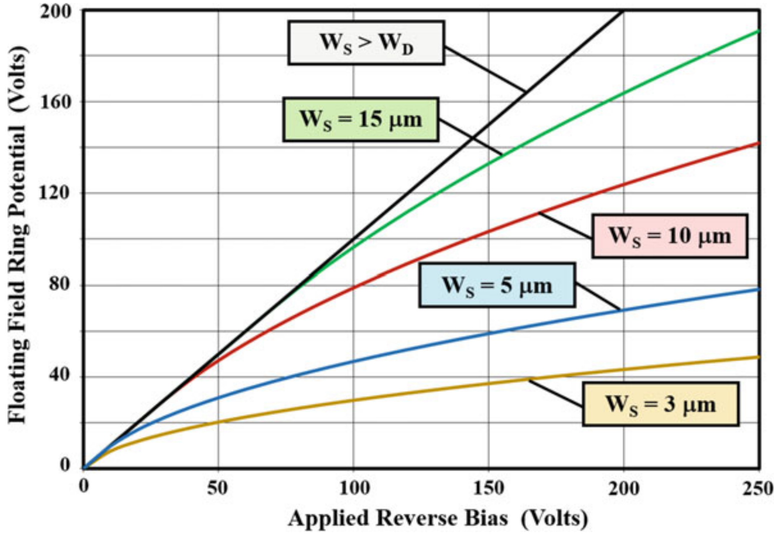

Fig. 3.21 Floating field ring potential for various field ring spaces

electric field at the main junction and floating field ring junction simultaneously become equal to the critical electric field for breakdown. Analysis of the breakdown voltage for the floating field ring termination [15] can be performed under the assumption that the electric field at the main junction is determined by the difference in voltage between the main junction and the floating field ring while the electric field at the floating field ring junction is governed by the cylindrical junction. Under these assumptions, the potential of the floating field ring (V_{FFR}) must be equal to the breakdown voltage of the cylindrical junction with the same radius of curvature and doping concentration in the drift region:

$$\frac{V_{FFR}}{BV_{PP}} = \frac{BV_{CYL}}{BV_{PP}} \tag{3.64}$$

The difference in the voltage between the main junction (V_M) and the floating field ring can be obtained by using the voltage distribution for a cylindrical junction given by Eq. (3.44) with $r = W_S$:

$$(V_M - V_{FFR}) = \frac{qN_D}{2\varepsilon_S}\left[\left(\frac{r_J^2 - W_S^2}{2}\right) + r_D^2 . \ln\left(\frac{W_S}{r_J}\right)\right] \tag{3.65}$$

Under breakdown, the potential of the main junction (V_M) becomes equal to the breakdown voltage of the floating field ring termination (BV_{FFR}). Making use of Eqs. (3.63), (3.65) and the basic relationship for the parallel-plane junction:

$$BV_{PP} = \frac{1}{2}E_C W_{PP} = \frac{qN_D}{2\varepsilon_S} W_{PP}^2 \tag{3.66}$$

to normalize the solution, it can be shown that:

$$\left(\frac{BV_{FFR} - BV_{CYL}}{BV_{PP}}\right) = \frac{1}{2}\left(\frac{r_J}{W_{PP}}\right)^2 - 0.96\left(\frac{r_J}{W_{PP}}\right)^{6/7} + 1.92\left(\frac{r_J}{W_{PP}}\right)^{6/7} \ln\left[1.386\left(\frac{W_{PP}}{r_J}\right)^{4/7}\right] \quad (3.67)$$

It is worth pointing out that this expression is valid under the assumptions that (a) the radius of curvature for the junction is small when compared with the depletion layer width at breakdown for the parallel-plane junction and (b) the floating field ring is located at an optimal spacing from the main junction. The normalized breakdown voltage calculated using this analytical formulation is compared with the breakdown voltage for the cylindrical junction in Fig. 3.22.

From Fig. 3.22, it can be observed that the breakdown voltage can be approximately doubled by the addition of a floating field ring to the cylindrical junction. This provides a powerful method for increasing the breakdown voltage with no additional processing steps because the floating field ring can be formed simultaneously with the main junction. This design requires precise location of the floating field ring at the optimum spacing from the main junction. An analytical solution for the optimal spacing [12] can be derived by solving for W_S in Eq. (3.65) with V_M equal to BV_{FFR} and V_{FFR} equal to BV_{CYL} and eliminating N_D by using Eq. (3.66):

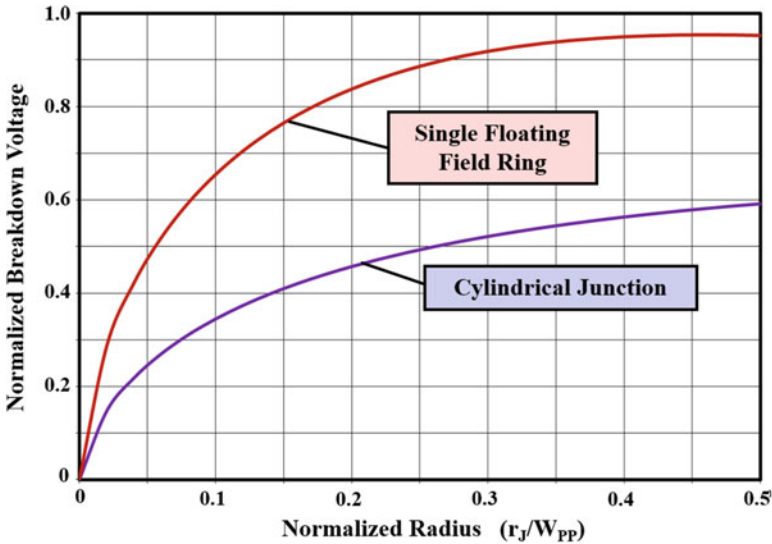

Fig. 3.22 Breakdown voltages for cylindrical junctions with a single floating field ring

$$W_S^2 - 2\sqrt{\frac{BV_{FFR}}{BV_{PP}}}W_{PP}W_S + \left(\frac{BV_{CYL}}{BV_{PP}}\right)W_{PP}^2 = 0 \quad (3.68)$$

This quadratic equation provides an elegant solution for the optimum field ring spacing in terms of the breakdown voltage of the cylindrical and floating field ring cases when the spacing is normalized to the depletion width of the parallel-plane junction at breakdown:

$$\frac{W_S}{W_{PP}} = \sqrt{\frac{BV_{FFR}}{BV_{PP}}} - \sqrt{\left(\frac{BV_{FFR}}{BV_{PP}}\right) - \left(\frac{BV_{CYL}}{BV_{PP}}\right)} \quad (3.69)$$

The normalized optimum spacing for the floating ring is a function of the ratio of the radius of curvature of the junction to the depletion layer width at breakdown for the parallel-plane junction because the normalized breakdown voltages in the above equation depend on this ratio. A plot for the normalized optimum spacing for the floating field ring is provided in Fig. 3.23. The optimum spacing becomes larger with increasing normalized radius of curvature for the junction. The optimum spacing is in the range of 0.15–0.35 times the depletion layer width for the parallel-plane junction at breakdown. For a doping concentration of 3.8×10^{14} cm^{-3} (previously used in the context of cylindrical junctions) and a junction depth of 5 μm, a normalized radius of curvature of 0.11 is obtained because the depletion layer width at breakdown is 47 μm. Using this value, an optimum spacing for the floating field ring is found to be 12 μm by using the analytical solution corresponding to a normalized value of 0.258.

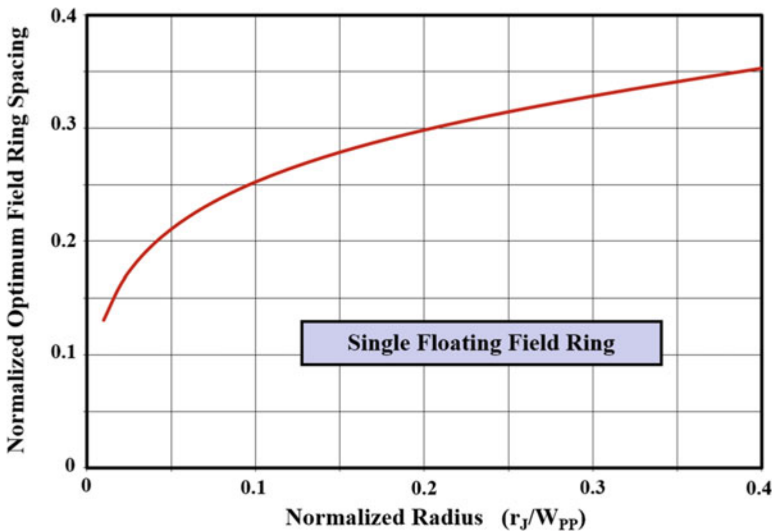

Fig. 3.23 Optimum spacing for a single floating field ring

Simulation Example

The results of two-dimensional numerical simulations are provided in this section for the case of a drift region with doping concentration of 3.8×10^{14} cm^{-3} to gain further insight into the operation of the cylindrical junction with floating field ring. At this doping concentration, the parallel-plane breakdown voltage was found to be 520 V with a depletion region thickness of 41 μm for the case of a P^+ region with a surface doping concentration of 1×10^{20} cm^{-3} and depth of 5 μm as discussed earlier. The simulations of the floating field ring termination were performed with various spacing between the main junction and the floating field ring. In all cases, the main junction had a width of 50 μm, and the width of the window for the floating field ring was maintained at 20 μm.

The potential of the floating field ring was monitored during the simulations as a function of the applied reverse bias to the main junction. As expected, the floating ring potential increases with increasing applied reverse bias as shown in Fig. 3.24. The potential of the floating field ring remains equal to the applied bias up to the corresponding vertical dashed line marked in the figure for each value for the spacing. This potential is very well predicted by the analytical solutions shown in Fig. 3.21. The potential increases more gradually, as described by the analytical model, when the applied bias extends the depletion region of the main junctions beyond the spacing of the floating field ring. The predictions of the analytical model, as shown in Fig. 3.21 in this domain of operation, are in good agreement with the simulation results for spacing above 5 μm providing credence to the model even though it was based upon simple one-dimensional considerations.

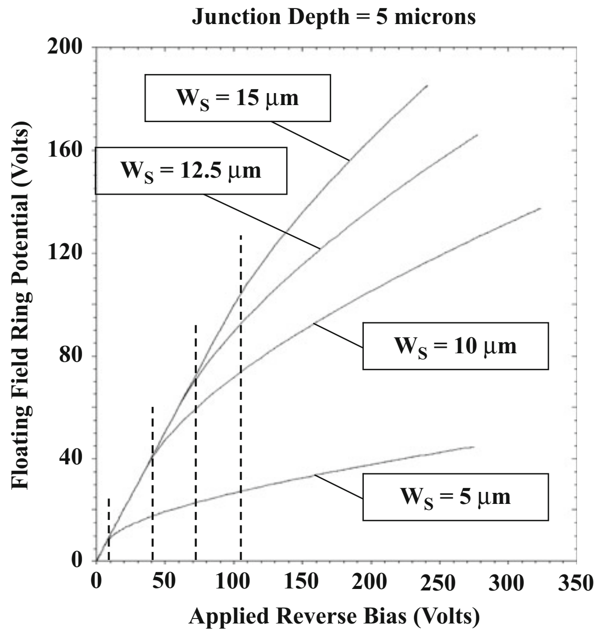

Fig. 3.24 Floating field ring potential determined by numerical simulations

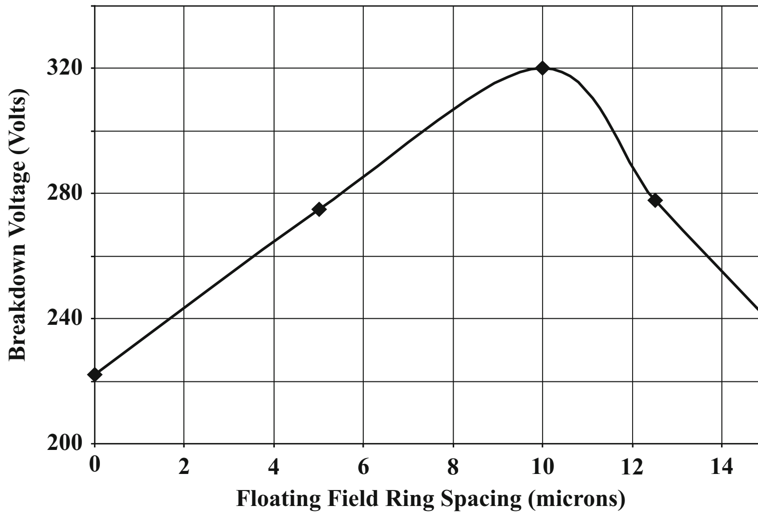

Fig. 3.25 Breakdown voltages of cylindrical junctions with a single floating field ring

The breakdown voltages of the cylindrical junction with floating field rings were obtained by performing simulations with various floating field ring spacing ranging up to 15 μm. The breakdown voltage was found to go through a maximum value as the floating field ring spacing was increased as shown in Fig. 3.25. The maximum breakdown voltage was found to be 320 V, which is 62% of the parallel-plane breakdown voltage. The normalized breakdown voltage (66% of the parallel-plane breakdown voltage) predicted by the analytical model for this case of normalized radius of curvature of 0.11 is in good agreement with the simulated value.

The optimum spacing for the floating field ring obtained from the simulations is 10 μm, which is 24% of the depletion layer width for the parallel-plane junction. The analytical model predicts an optimum spacing of 0.26 times the depletion layer width for the parallel-plane junction. Consequently, the analytical model provides an excellent tool for choice of the placement for the floating field ring. This spacing can then be further refined by performing two-dimensional numerical simulations.

In order to gain further insight into the impact of an optimum placement of the floating field ring, the electric field distribution is shown in Fig. 3.26 for three values for the field ring spacing. In each case, the electric field has been plotted along the surface for various reverse bias voltages applied to the cathode. In the case of the smallest spacing of 5 μm, the electric field increases more rapidly at the edge of the floating field ring located at 90 μm. This results in breakdown occurring at the edge of the floating field ring at a lower reverse bias voltage. In the case of the largest spacing of 15 μm, the electric field increases more rapidly at the edge of the main junction located at 55 μm. This results in breakdown occurring at the main junction at a lower reverse bias voltage. For the optimum floating field ring spacing of 10 μm, the maximum electric field at the edge of the field ring is equal to the maximum electric field developed at the main junction. In this case, the breakdown voltage is

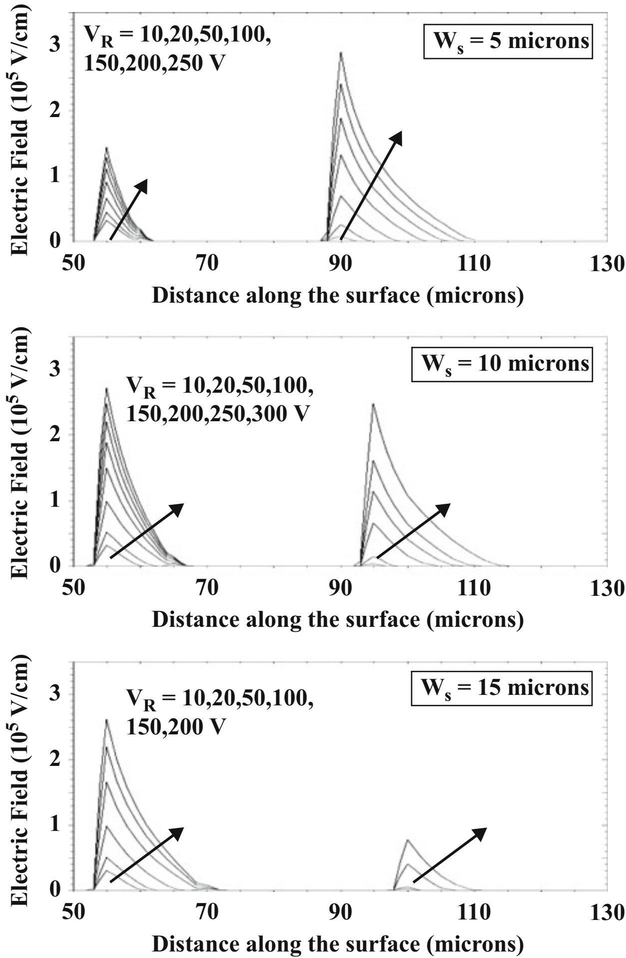

Fig. 3.26 Electric field profiles in cylindrical junctions with single floating field rings with various spacing

maximized with breakdown occurring simultaneously at the edge of the floating field ring and the edge of the main junction.

A three-dimensional view of the electric field distribution is shown at a reverse bias of 300 V in Fig. 3.27 for the case of a cylindrical junction with a single floating field ring located at 10 μm from the main junction. It can be observed that the electric fields at the edges of the main junction and the field ring are equal in magnitude indicating the floating field ring is located at an optimum distance from the main junction. However, the electric fields at these edges are much larger than in the parallel-plane portion of the main junction. This enhancement of the electric field is responsible for the breakdown voltage for even the optimum floating field ring design being less than the parallel-plane breakdown voltage.

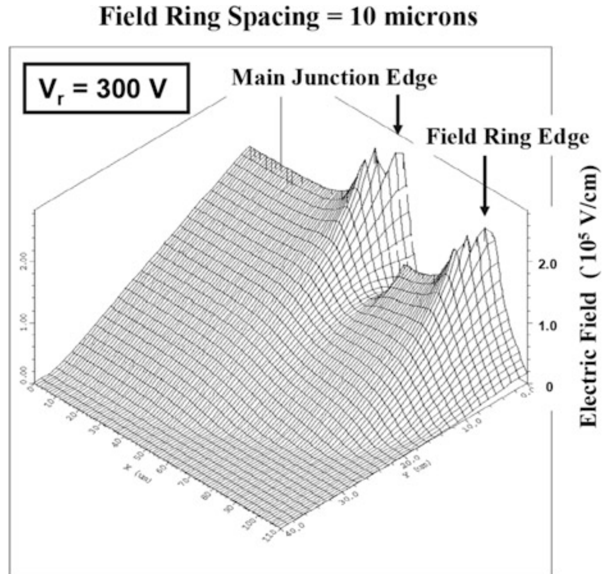

Fig. 3.27 Three-dimensional view of the electric field distribution for a cylindrical junction with a single floating field ring

Impact of Fixed Oxide Charge

The breakdown voltage of the edge termination with floating field rings has been found to be sensitive to the presence of fixed oxide charge in the passivation layer between the main junction and the floating field ring. This can be understood by considering the influence of the oxide charge on the depletion layer under the passivation oxide as schematically illustrated in Fig. 3.28. The presence of a negative charge in the oxide compensates the positive charge at the ionized donors producing an extension of the depletion layer along the surface. The presence of a positive charge has the opposite effect on the depletion layer at the surface. In the case of a cylindrical junction, the presence of a positive charge in the oxide, which occurs in thermally grown oxide layers on silicon, enhances the junction curvature and electric field resulting in a reduction of the breakdown voltage. In the case of the edge termination with a floating field ring, the presence of the positive charge in the oxide perturbs the potential acquired by the floating field ring. This disturbs the electric field distribution for an optimally spaced floating field ring designed without taking this charge into account.

Simulation Example
Numerical simulations for the case of floating field ring spacing of 10 μm were repeated after inclusion of an oxide charge of 1×10^{11} cm^{-2}. The breakdown voltage obtained by the simulations was 256 V, which is considerably lower than before inclusion of the oxide charge. This can be understood by examination of the electric field within the structure as shown in Fig. 3.29 at a reverse bias of 250 V. It can be seen that the electric field at the edge of the main junction has been enhanced

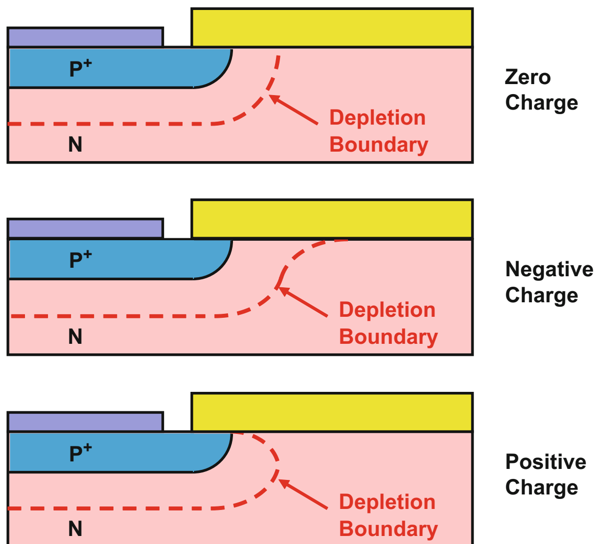

Fig. 3.28 Impact of fixed oxide charge on the depletion boundary for a cylindrical junction

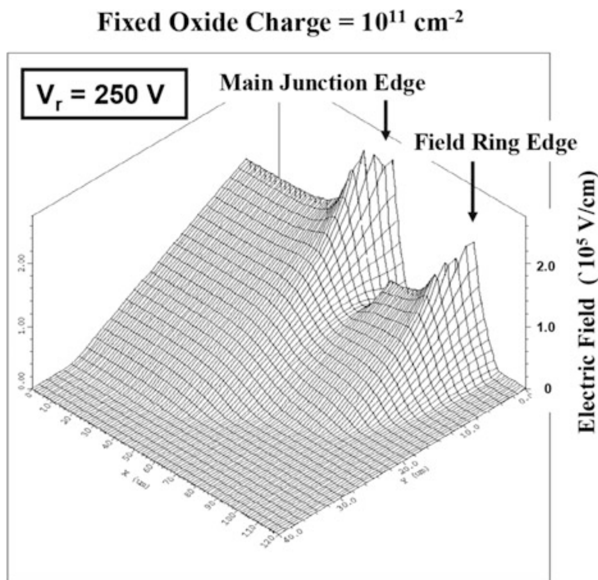

Fig. 3.29 Three-dimensional view of the electric field distribution for a cylindrical junction with a single floating field ring: impact of fixed oxide charge

in relation to the electric field at the edge of the floating field ring due to the positive charge in the oxide.

In principle, it is possible to account for the presence of the oxide charge during the optimization of the design of the location of the floating field ring. Unfortunately, the charge in the thermally grown field oxide during the fabrication of power devices can vary from wafer to wafer and even across a wafer by as much as 10^{11} cm^{-2}.

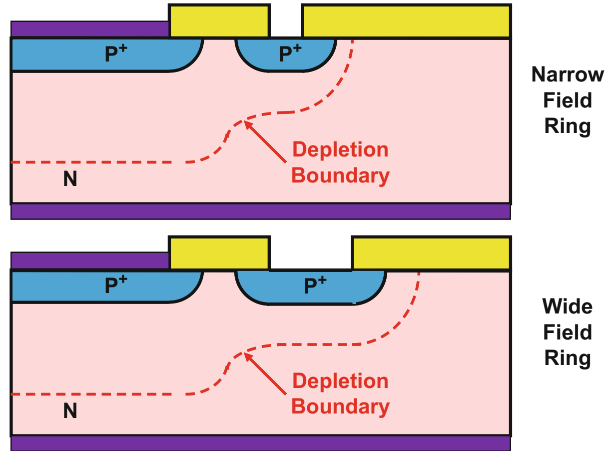

Fig. 3.30 Impact of the width of the floating field ring

The results of the simulations demonstrate that the breakdown voltage for an edge termination with single floating field ring can be significantly reduced due to the presence of this charge. This can produce a wide distribution in the breakdown voltages of the power devices which is detrimental to getting a high yield during their manufacturing. This problem can be mitigated by using multiple floating field rings.

Floating Field Ring Width

It is advantageous to reduce the width of the floating field ring as much as possible from the point of view of saving space occupied by the edge termination at the periphery of the power devices. However, it has been found that the effectiveness of the floating field ring in terms of improving the breakdown voltage of the cylindrical junction is compromised if its width becomes too small. This is schematically illustrated in Fig. 3.30, where the depletion layer shape is shown for a narrow and wide floating field ring. The electric field becomes enhanced at the edge of the floating field ring when its width is too small. It is necessary to make the width of the floating field ring at least equal to the depletion width (W_{PP}) of the parallel-plane junction at breakdown to achieve its full effectiveness.

3.6.3 Planar Junction with Multiple Floating Field Rings

In the case of devices that are designed to support less than 50 V, the depletion width is relatively small, and a single floating field ring is usually sufficient to provide a breakdown voltage close to that for the parallel-plane junction even when the

junction depth is less than 5 μm. However, as the breakdown voltage of the device (and consequently the depletion width) increases, the breakdown voltage for a cylindrical junction with a single floating field ring becomes much lower than that for the parallel-plane junction. This problem can be overcome by the placement of multiple floating field rings around the main junction.

The electric field developed at the edge of the single floating field ring can be reduced by the addition another floating field ring that surrounds it. This favors a closer spacing for the first floating field ring from the main junction than the optimum spacing with a single floating field ring. This approach can be applied to each additional floating field ring around the main junction. In addition, the width of the floating field rings can be reduced when they are placed away from the main junction because the depletion width is smaller under them.

Two approaches to designing the edge termination with multiple floating field rings have evolved. In the first approach, shown in Fig. 3.31, both the floating field ring width and the spacing between the field rings is reduced with increasing distance from the main junction. This produces a gradual variation of the depletion width at the termination which is favorable for reducing electric fields. In this approach, the width of the outer rings is reduced in proportion to the underlying depletion layer width because this reduces the space occupied by the termination. The optimization of the spacing between the rings requires a precise knowledge of the charge in the field oxide. With an optimum design, the electric field at the outer edge of all the field rings is equal so that avalanche breakdown occurs simultaneously at these locations.

In the second approach shown in Fig. 3.32, all the floating field rings are equally spaced and their widths are made equal. This allows accommodating more floating field rings within a given space on the edge of the chip. This produces a finer gradation of the depletion region at the edge resulting in reducing the electric field. The presence of more floating field rings is believed to reduce the impact of variation in the oxide charge.

In principle, the use of multiple floating field rings allows increasing the breakdown voltage of planar junctions arbitrarily close to the parallel-plane breakdown voltage by the addition of a very large number of rings. In practice, there is a diminishing benefit in terms of increasing the breakdown voltage from the addition

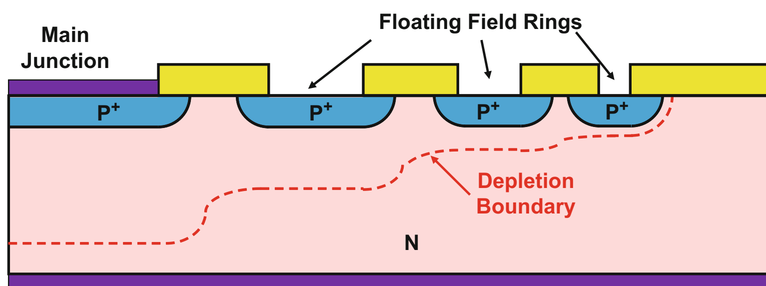

Fig. 3.31 Multiple floating field ring termination with graded spacing and width

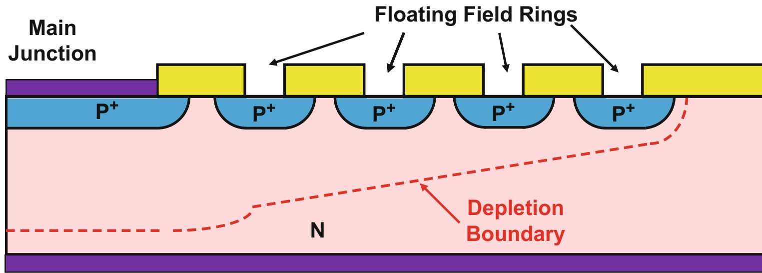

Fig. 3.32 Multiple floating field ring termination with equal spacing and width

Fig. 3.33 Planar junction with biased field plate over the field oxide

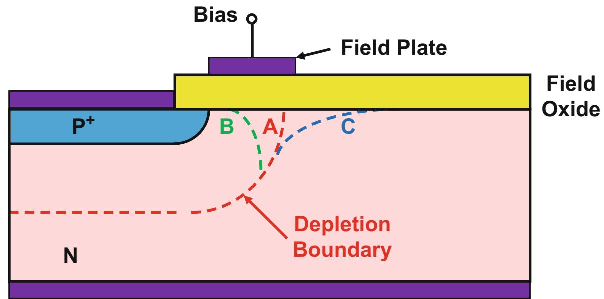

of floating rings, while more space is occupied by the edge termination resulting in a larger die size and cost. Although planar edge terminations with up to ten floating field rings have been reported, it is usually practical to use only up to three floating field rings to enhance the breakdown voltage.

3.6.4 Planar Junction with Field Plate

A planar junction with a metal field plate located at its edge over the field oxide is illustrated in Fig. 3.33. The electric field at the edge of a planar junction can be modulated by the application of a bias voltage to the metal [16]. With no bias voltage applied to the field plate, the depletion region boundary has the form indicated by case A for the cylindrical junction. When a positive bias is applied to the field plate with respect to the N-type substrate, it attracts electrons toward the surface. This shrinks the extension of the depletion layer along the surface as indicated by case B. This will enhance the electric field at the junction producing a reduction in the breakdown voltage. On the other hand, if a negative bias is applied to the field plate, it repels electrons away from the surface. This will produce an expansion of the depletion region at the surface as indicated by case C. This will result in a reduction of the electric field at the junction leading to an increase in the breakdown voltage.

It has been found [16] that the breakdown voltage of the diode with the field plate (BV_{FP}) is related to the magnitude of the negative bias (V_{FP}) applied to the field plate:

$$BV_{FP} = mV_{FP} + K \tag{3.70}$$

where m and K are constants. The value for m is close to unity especially for smaller field oxide thicknesses.

With the application of a sufficient potential to the field plate, it is possible to approach the breakdown voltage of a parallel-plane junction. However, it is not practical to provide a separate bias to a field plate in the case of discrete power devices because of the additional package terminal as well as the cost associated with the bias circuit. An alternative approach is to form the field plate by extending the contact metal for the P^+ region over the field oxide at the edge of the junction as shown in Fig. 3.34. In this case, the application of a negative voltage to the P^+ region to reverse bias the P-N junction also provides a negative bias to the field plate. This produces an expansion of the depletion region along the surface as illustrated in the figure. The resulting reduction in the electric field at the cylindrical junction (point A) will increase the breakdown voltage. However, a high electric field can be produced at the edge of the field plate at point B. This can result in a reduction of the breakdown voltage.

Analysis of the breakdown at the edge of the field plate can be performed by treating the edge of the field plate as a cylindrical junction with the oxide under the field plate serving as the highly doped side of the junction. The difference in the dielectric constants for silicon dioxide and silicon must be taken into account when making this analogy. In accordance with Gauss's law, the electric field in the semiconductor is related to the electric field in the oxide in proportion to their permittivity. Based upon this, the junction depth corresponding to an oxide thickness of t_{OX} is given by:

$$x_J = \left(\frac{\varepsilon_{Si}}{\varepsilon_{OX}}\right) t_{OX} \approx 3t_{OX} \tag{3.71}$$

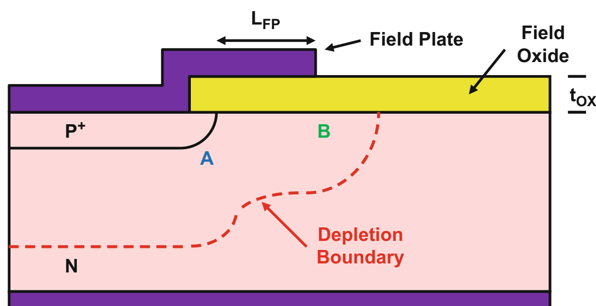

Fig. 3.34 Planar junction with metal field plate over the field oxide

The breakdown voltage at the field plate for a field oxide thickness of 1 μm would be equivalent to the breakdown voltage of a cylindrical junction with a depth of 3 μm. Using this junction depth, the breakdown voltage can be obtained by using the analytical formulations developed for cylindrical junctions. However, it is important to avoid sharp corners at the field plate to prevent degradation of the breakdown voltage to that for a spherical junction with the same junction depth. For the case of a doping concentration of 3.8×10^{14} cm^{-3} in the N-type substrate, the breakdown voltage at the edge of the field plate can be determined to be 174 V using the cylindrical junction analysis. This value is pessimistic as shown by the results of two-dimensional numerical simulations.

Simulation Example

The results of two-dimensional numerical simulations are provided in this section for the case of a drift region with doping concentration of 3.8×10^{14} cm^{-3} to gain further insight into the operation of the cylindrical junction with a field plate. At this doping concentration, the parallel-plane breakdown voltage was found to be 520 V with a depletion region thickness of 41 μm for the case of a P^+ region with a surface doping concentration of 1×10^{20} cm^{-3} and depth of 5 μm. The simulations of the field plate termination were performed with various lengths (L_{FP}) of the field plate and different field oxide thickness (t_{OX}). Note that the length of the field plate is defined as its extension from the edge of the junction (see Fig. 3.34) and not the edge of the diffusion window. In all cases, the main junction had a width of 50 μm.

In the absence of the field plate, the breakdown voltage of the cylindrical junction was found to be 220 V. For the case of a field oxide thickness of 1 μm, the breakdown voltage was found to increase upon the addition of the field plate. The increase in the breakdown voltage is dependent upon the length of the field plate as shown in Fig. 3.35. It can be seen that extension of the field plate beyond 15 μm will not produce enhancement of the breakdown voltage for this case. The addition of the field plate provides a 40% improvement in the breakdown voltage over that for the cylindrical junction. This is comparable to the improvement in breakdown voltage obtained by using a single optimally spaced field ring.

A three-dimensional view of the electric field distribution within the silicon is shown in Fig. 3.36 for the case of cylindrical junction with a field plate at a reverse bias of 300 V. The field plate had a length of 10 μm and the field oxide thickness was 1 μm. The electric field in the semiconductor reaches a magnitude of about 3×10^5 V/cm at a much larger voltage when compared with the cylindrical junction (see Fig. 3.17). The electric field at the edge of the field plate can be seen to be slightly larger than at the edge of the cylindrical junction.

The breakdown voltage of the cylindrical junction with the field plate termination is also dependent upon the thickness of the field oxide. This is demonstrated in Fig. 3.37 for case of a junction depth of 5 μm and a field plate length of 10 μm. A field oxide thickness of 1 μm is necessary to take full advantage of the incorporation of the field plate. The breakdown voltage degrades when the field oxide thickness is reduced below this value. In the case of an oxide thickness of 0.25 μm, the

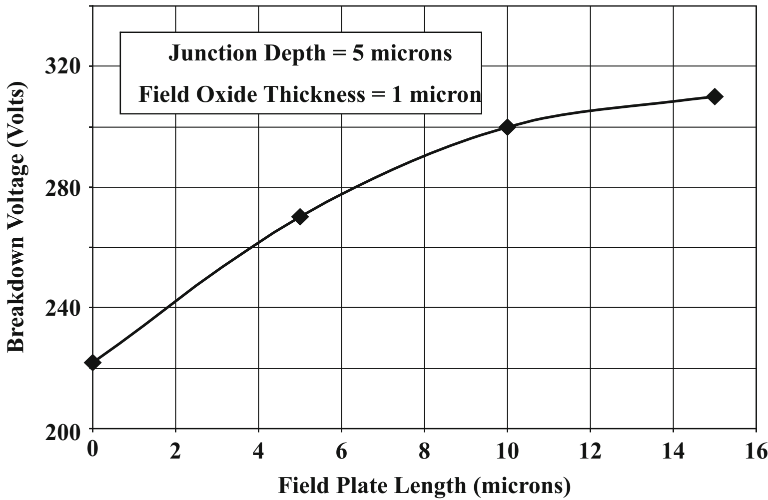

Fig. 3.35 Breakdown voltages of cylindrical junctions with a field plate

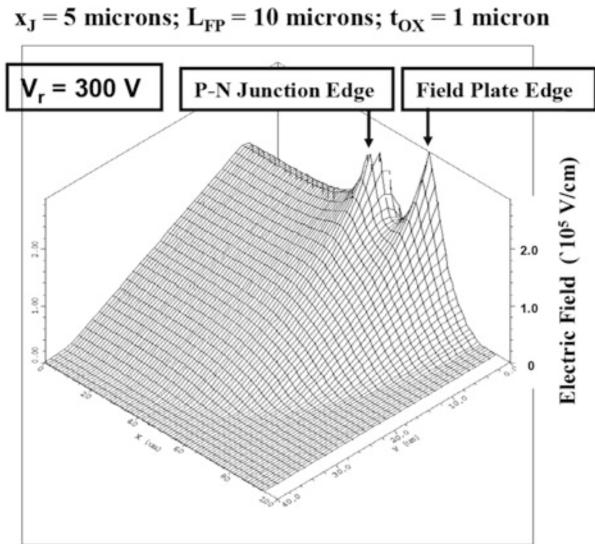

Fig. 3.36 Electric field distribution in a cylindrical junction with a field plate

breakdown voltage is reduced to 205 V which is lower than that for the cylindrical junction. This reduction is due to the enhanced electric field at the edge of the field plate as shown in Fig. 3.38. It can be seen that this electric field exceeds that at the junction resulting in avalanche breakdown being initiated at the edge of the field plate. Although this is consistent with the predictions of the analytical model, the magnitude of the breakdown voltage is significantly larger.

The effectiveness of the field plate in improving the breakdown voltage of cylindrical junctions is also dependent upon the junction depth. The field plate has

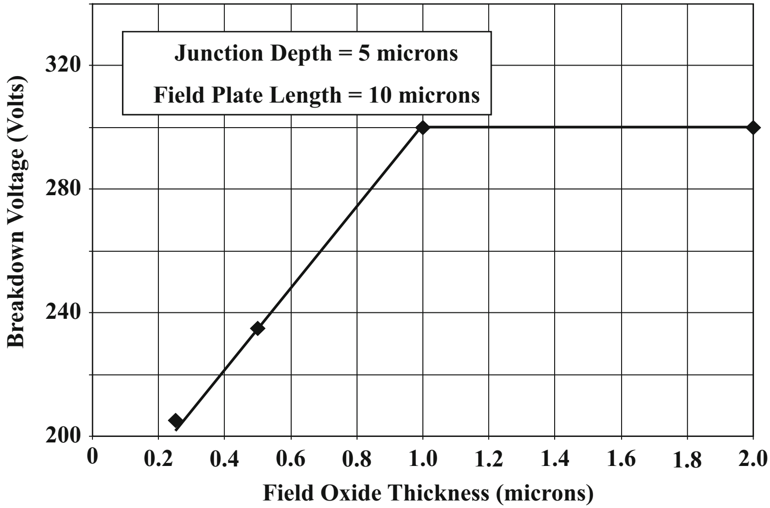

Fig. 3.37 Breakdown voltages of cylindrical junctions with a field plate

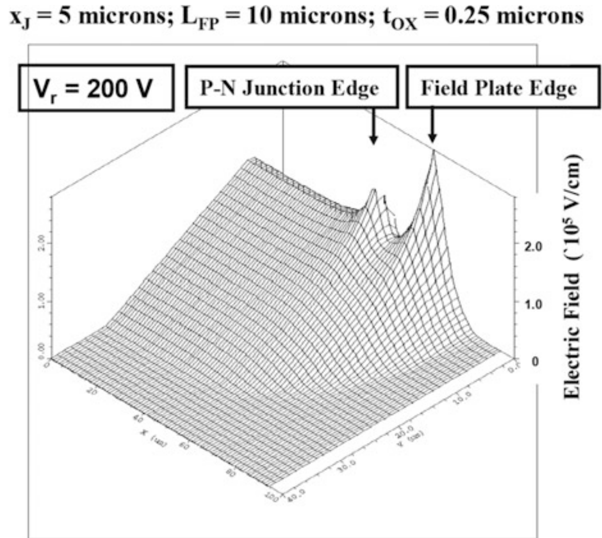

Fig. 3.38 Electric field distribution in a cylindrical junction with a field plate

a stronger impact on the electric field for shallower junction depths due to its proximity. As an example, when the junction depth was reduced from 5 to 2 μm while maintaining the same field oxide thickness of 1 μm and field plate length of 10 μm, the breakdown voltage obtained by the numerical simulations was found to be 280 V. In this case, the breakdown voltage is enhanced from 160 V for the cylindrical junction by nearly a factor of 2 times.

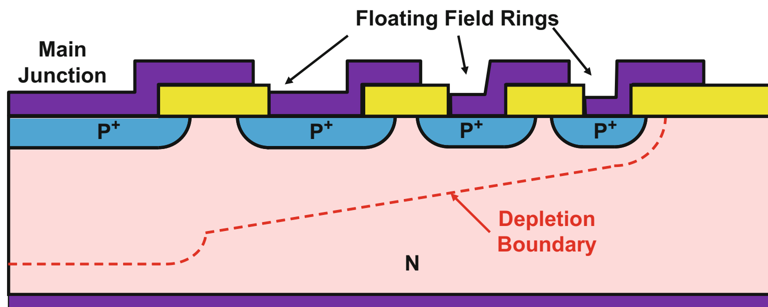

Fig. 3.39 Multiple floating field ring termination with field plates

3.6.5 Planar Junction with Field Plates and Field Rings

A popular edge termination design for power devices combines the effectiveness of the multiple floating field rings with field plates. The field plates are designed to extend over the space between the junctions as shown in Fig. 3.39. The field plates reduce the electric field at the edges of all the junctions and also prevent mobile ions from entering the field oxide. Mobile ions can be introduced at the surface of power devices during the packaging operations. It has been found that the presence of mobile ions can produce instabilities (called *walk-out*) in the breakdown voltage because they are redistributed by the electric field.

The floating field ring termination is the most practical solution for improving the breakdown voltage of power devices with voltage ratings up to 1500 V. These devices include power rectifiers, power MOSFETs, and IGBTs. Until the development of this approach, it was common practice to etch the region between devices on a wafer to expose the junction followed by passivation using dielectrics deposited on the etched surface. This method, called *mesa termination*, was difficult to control resulting in wide variability in the breakdown voltage. The evolution of the planar junction termination with floating field rings brought about a major improvement in the manufacturability of power devices.

3.6.6 Bevel Edge Terminations

Power rectifiers and thyristors with voltage ratings above 2000 V are required for high power systems such as power distribution networks. Due to the high power levels encountered in these applications, the current rating for the devices is also very large (see Fig. 1.2). Consequently, these types of devices are manufactured with an entire wafer serving as a single device. In addition, in order to improve the breakdown voltage capability, it is advantageous to prepare deep diffusions with low surface concentration because this creates a graded doping profile at the junction.

A substantial portion of the applied reverse bias can then be supported within the diffused region which enhances the breakdown voltage.

The diffusion coefficient for boron is too low even at 1200 °C (see Fig. 2.21) to enable the fabrication of junctions with depths of 50–100 μm. It is necessary to utilize aluminum and gallium as P-type dopants to prepare such deep junctions with low surface concentrations by performing the diffusion at 1200 °C in a sealed tube. The masking of such diffusions was not considered to be possible until the 1970s making it impossible to fabricate planar junctions. A process for the fabrication of planar junctions was eventually developed by using silicon nitride as the masking layer [17]. Meanwhile, techniques were developed for reducing the electric field at the edges of the wafer by using a bevel. The process of beveling consists of removal of silicon at the edges of the wafer at a precisely controlled angle. The beveling of the edges has been demonstrated to enhance the breakdown voltage by reducing the electric field at the edges when compared with cutting the wafer orthogonal to the surface.

Two configurations for the bevel edge termination have been found to be successful for applications in power rectifiers and thyristors. The positive bevel configuration, shown in Fig. 3.40, is preferable for the termination of the single high-voltage junction within high-voltage power rectifiers. It is also utilized to terminate the anode junction in high-voltage thyristors to obtain a stable reverse blocking capability. In general, a positive bevel angle is defined as one where more material is removed from the edge when progressing from the heavily doped side to the lightly doped side of the P-N junction

The negative bevel termination, shown in Fig. 3.41, is used for the termination of the forward blocking junction in thyristors. In general, a negative bevel angle is defined as one where more material is removed from the edge when progressing from the lightly doped side to the heavily doped side of the P-N junction. As illustrated in the figure, a relatively shallow angle is required to obtain stable performance with the negative bevel termination. These terminations are discussed in more detail below.

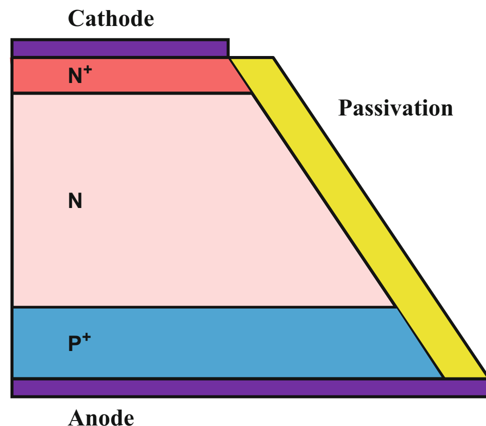

Fig. 3.40 Power rectifier with positive bevel edge termination

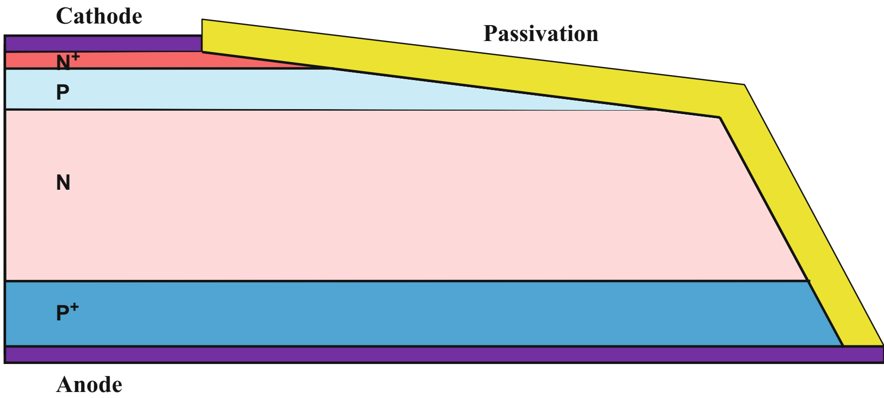

Fig. 3.41 Power thyristor with upper junction negative bevel edge termination

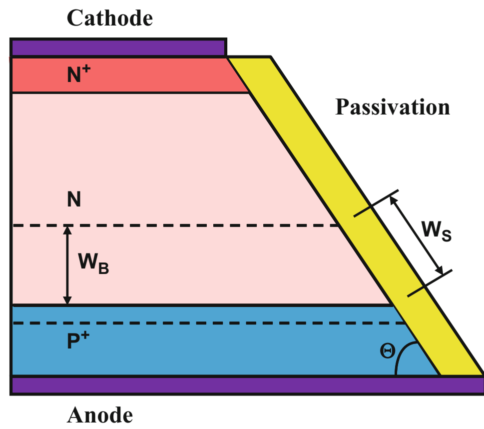

Fig. 3.42 Positive bevel edge termination: Model A

Positive Bevel

The positive bevel edge termination with a bevel angle θ is illustrated in Fig. 3.42 with a simple model for the positions of the depletion regions on both sides of the P-N junction shown by the dashed lines. In this Model A, the depletion regions are assumed to retain a flat shape all the way to the bevel edge. The width of the depletion region along the beveled surface (W_S) is then related to the depletion width of the P-N junction in the bulk (W_B) by:

$$W_S = \frac{W_B}{\sin(\theta)} \tag{3.72}$$

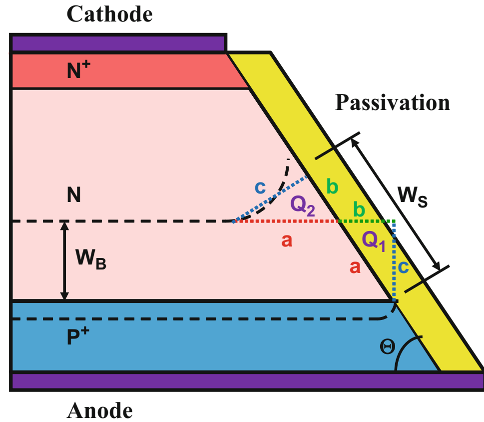

Fig. 3.43 Positive bevel edge termination: Model B

Since the same voltage is being supported across the P-N junction in the bulk and at the beveled surface, the maximum electric field at the surface of a positive bevel (E_{mPB}) is related to the maximum electric field in the bulk (E_{mB}) by:

$$E_{\mathrm{mPB}} = E_{\mathrm{mB}}\left(\frac{W_{\mathrm{B}}}{W_{\mathrm{S}}}\right) = E_{\mathrm{mB}} \sin(\theta) \tag{3.73}$$

This simple model overestimates the magnitude of the electric field at the surface of the positive bevel because it does not take into account the impact of the removal of the charge due to the bevel.

The influence of the bevel on the depletion region at the edges is included in Model B. A positive bevel edge termination is illustrated in Fig. 3.43 for this case with the positions of the depletion regions on both sides of the P-N junction shown by the dashed lines. In order to maintain charge balance between the P- and N-sides of the junction, the depletion region in the P-type region is reduced at the edge until it is pinned at the junction. At the same time, the depletion region on the N-type region expands at the edge to compensate for the removal of the charge labeled Q_1 in the figure. The expansion of the depletion region in the N-type region near the edge can be represented by a right-angled triangle with an area Q_2 which is equal to the removed charge Q_1.

The width of the depletion region along the beveled surface (W_{S}) can be related to the depletion width of the P-N junction in the bulk (W_{B}). The hypotenuse (labeled "a" in the figure) of the two right-angled triangles for the charges Q_1 and Q_2 must be equal because the triangles have equal area and share a common angle. The other sides are also related as indicated by the letters "b" and "c" in the figure. Since the dimension "c" is equal to the depletion width in the bulk (W_{B}):

$$a = \frac{W_{\mathrm{B}}}{\sin(\theta)} \tag{3.74}$$

and

$$b = \frac{W_B}{\tan(\theta)} \tag{3.75}$$

The width of the depletion region along the beveled surface is then given by:

$$W_S = a + b = W_B\left(\frac{1}{\sin(\theta)} + \frac{1}{\tan(\theta)}\right) \tag{3.76}$$

Since the same voltage is being supported across the P-N junction in the bulk and at the beveled surface, the maximum electric field at the surface of a positive bevel (E_{mPB}) is given by:

$$E_{mPB} = E_{mB}\left(\frac{W_B}{W_S}\right) = E_{mB}\left(\frac{\sin(\theta)}{1 + \cos(\theta)}\right) = E_{mB}\tan\left(\frac{\theta}{2}\right) \tag{3.77}$$

The variation of the normalized surface electric field to the bulk value predicted by this equation is shown in Fig. 3.44 as a function of the positive bevel angle together with the predictions of the simple Model A. It can be seen that a significant reduction of the surface electric field can be achieved by using the positive bevel. With a positive bevel angle of 45°, the surface electric field is about 40% of the bulk value. It has been found that surface breakdown can occur at lower electric fields than in the bulk due to the presence of imperfections. However, a reduction in the electric field by 40% is usually sufficient to shift the breakdown from the surface to the bulk. This ensures stable operation while maximizing the breakdown voltage to that for a parallel-plane junction. It is worth pointing out that the positive bevel edge

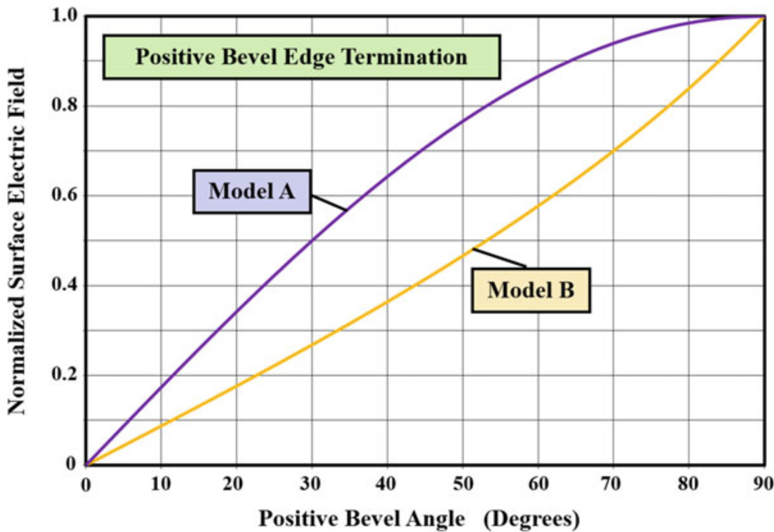

Fig. 3.44 Surface electric field in the positive bevel edge termination

termination is the only technique that has been found to ensure that the surface electric field is well below that in the bulk of the device.

Two-dimensional numerical simulations [18] of the positively beveled junction have confirmed the reduction of the electric field at the surface. The maximum surface electric field has been extracted for a variety of positive bevel angles using simulations with different background doping concentration for the N-type region and various doping profiles for the P-type region [19]. The normalized surface electric field obtained from the simulations has a remarkably similar behavior (shown in Fig. 3.44 with Model B) to that obtained with the simple analytical method described above. These results indicate that the optimum positive bevel angle is in the range of 30°–60°. Larger angles are not recommended because of the enhanced surface electric field, while smaller angles lead to wasted space on the edge of the wafer.

The positive bevel angle for high-voltage power devices, such as power rectifiers and thyristors, is constructed by first attaching the wafer to a molybdenum heat sink. A nozzle is used to bombard the edge of the wafer (while it is rotated) with an abrasive powder (called grit). The angle of the nozzle in relation to the wafer surface determines the positive bevel angle. The damage caused to the silicon crystal by the grit blasting must be removed prior to the passivation of the surface. This technique is commonly used to terminate the high-voltage blocking junction in power rectifiers and the reverse blocking junction in high-voltage power thyristors.

Simulation Example

The results of two-dimensional numerical simulations are provided in this section for the case of a drift region with doping concentration of 5×10^{13} cm^{-3} to gain further insight into the operation of the positive bevel junction termination. At this doping concentration, the parallel-plane breakdown voltage was found to be 3000 V with a depletion region thickness of 300 μm for the case of a P^+ region with a surface doping concentration of 1×10^{19} cm^{-3} and depth of 50 μm. These values are representative of the anode junction in high-voltage thyristors to provide its reverse blocking capability. The simulations of the positive bevel termination were performed with various bevel angles ranging from 15° to 90°. All the structures had an oxide layer over the bevel surface as the passivation.

The reduction of the maximum surface electric field obtained from the numerical simulations is shown in Fig. 3.45 for the various bevel angles. Although the surface electric field is slightly larger than predicted by the analytical Model B, the results of the simulations clearly demonstrate the benefits of using a positive bevel angle as a termination for high-voltage, large area devices. The reduction of the surface electric field predicted by Model B is more than that indicated by the simulations because the model does not account for the extra charge created by the positive bevel within the diffused P^+ side of the junction. Based upon the results of the simulations, a positive bevel angle of 45° is recommended and commonly used for power devices.

The electric field profiles along the surface of the bevel obtained from the simulations are compared with the electric field profile in the bulk (dashed line) in Fig. 3.46. As expected, the electric field in the bulk has a maxima located at the

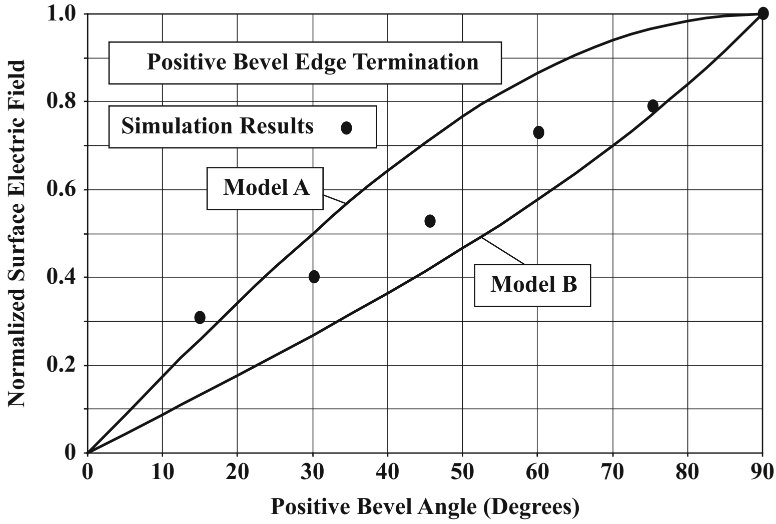

Fig. 3.45 Maximum surface electric field with a positive bevel termination

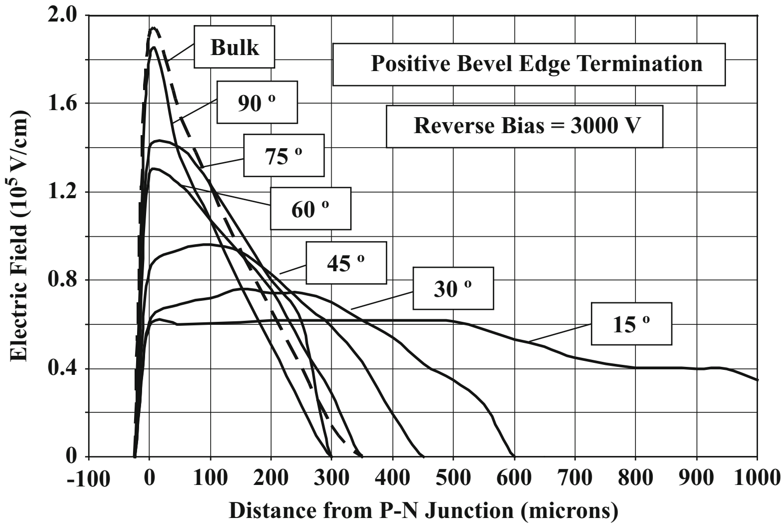

Fig. 3.46 Electric field profiles in a positive bevel termination

junction with a magnitude of 1.9×10^5 V/cm at a reverse bias of 3000 V. The electric field profile at the surface is similar in nature for a bevel angle of 90°. However, when the positive bevel angle is reduced, the peak of the surface electric field shifts away from the junction. Since the reverse bias voltage is supported over a larger distance along the surface, the magnitude of the maximum electric field is also

smaller than that in the bulk. This redistribution of the electric field is responsible for suppressing surface breakdown in the case of the positive bevel termination ensuring that the P-N junction is able to support the parallel-plane breakdown voltage.

Negative Bevel

A negative bevel is defined as one in which the area decreases when proceeding from the lightly doped side to the highly doped side of the P-N junction. Since the negative bevel removes more charge from the P^+ side of the junction than the N-side, the depletion region expands on the P-side and contracts on the N-side at the surface as illustrated in Fig. 3.47. The expansion of the depletion region on the P-side is relatively small due to the high doping concentration of the diffused region. Consequently, the width of the depletion region at the surface (W_S) is smaller than the depletion width in the bulk (W_B) for a negatively beveled junction. This implies that the electric field at the surface will be larger than in the bulk for this termination leading to unstable surface breakdown. It is, therefore, counterintuitive to make use of negative bevel edges in power devices.

A reduction of the surface electric field can be obtained by using a negative bevel angle of sufficiently small value in combination with a highly graded diffused side of the junction. The doping concentration of the P-base region in high-voltage power thyristors has to be reduced in order to obtain a sufficiently large current gain for the inherent N-P-N transistor within the four-layer structure. This provides an opportunity to use a negative bevel to terminate the forward blocking junction in these devices as illustrated in Fig. 3.41.

In order to analyze the electric field at the surface of a negative bevel junction, consider the P-N junction shown in Fig. 3.48 with the depletion region boundaries indicated by the dashed lines. The removal of more charge on the heavily doped side of the junction produces a reduction of the depletion layer width on the lightly doped N-side of the junction at the edges. For a shallow bevel angle, it has been reported

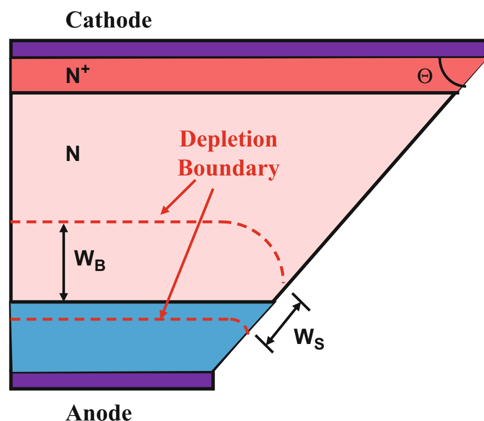

Fig. 3.47 Negative bevel edge termination

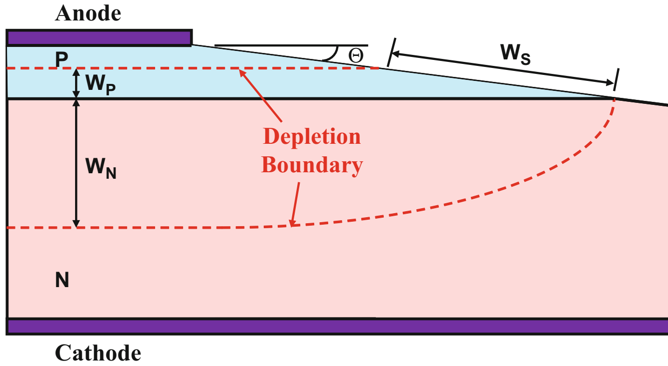

Fig. 3.48 Negative bevel edge termination with graded doping profile on the diffused side of the junction

[20] that the depletion region gets pinned at the junction located at the bevel surface. At the same time, the depletion region extends along the surface on the diffused side of the junction in order to compensate for the charge removed by the bevel. This extension of the depletion region on the diffused side of the junction is strongly dependent on the doping profile. A low concentration gradient for the P-region favors a greater extension of the depletion region resulting in a reduction of the surface electric field. Such shallow gradients can be produced by forming very deep junction with low surface concentrations using aluminum as the dopant.

For the model as depicted in Fig. 3.48, the extension of the depletion region along the surface (W_S) is given by:

$$W_S = \frac{W_P}{\sin(\theta)} \tag{3.78}$$

where W_P is the depletion width on the diffused side of the junction. Since the same voltage is being supported across the P-N junction in the bulk and at the beveled surface, the maximum electric field at the surface of a negative bevel (E_{mNB}) is given by:

$$E_{mNB} = E_{mB}\left(\frac{W_N}{W_S}\right) = E_{mB}\frac{W_N}{W_P}\sin(\theta) \tag{3.79}$$

The variation of the normalized surface electric field to the bulk value predicted by this equation is shown in Fig. 3.49 as a function of the negative bevel angle for the case of various values of W_N/W_P. It can be seen that a significant reduction of the surface electric field can be achieved by using a very shallow negative bevel angle. For instance, the surface electric field can be reduced to 50% of the bulk value for a negative bevel angle of 2.5° when W_N/W_P is 10. Such shallow bevel angles can be fabricated by using special wafer lapping equipment that allows precise adjustment of the angle between the wafer surface and the polishing pad. A space of 1–2 mm is consumed by the negative bevel at the perimeter of the wafer resulting in a small loss in the active area for current conduction.

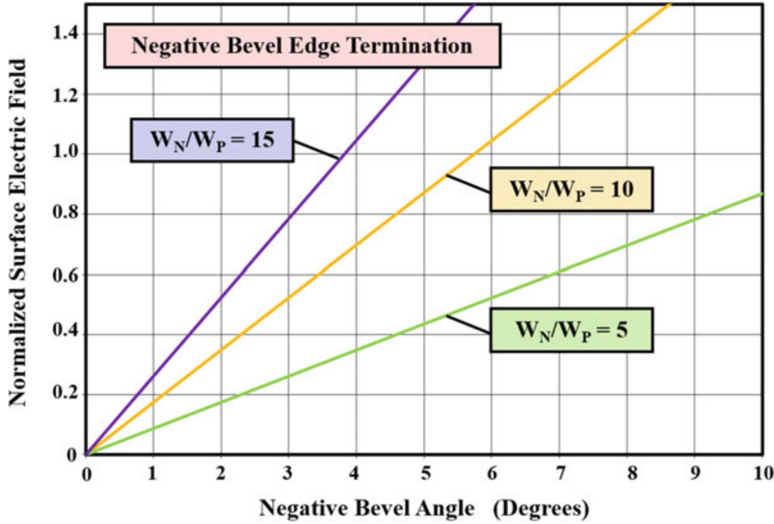

Fig. 3.49 Reduction of the maximum surface electric field with a negative bevel termination

It has been experimentally observed that the breakdown voltage of a junction terminated with a negative bevel is lower than that predicted for the parallel-plane junction. This was discovered to be due to the presence of an enhanced electric field in the bulk in the vicinity of the bevel surface [17]. Consequently, although the breakdown voltage can be stabilized by the reduction of the surface electric field with a negative bevel, its magnitude is below that of the parallel-plane junction. Negative bevels are only used for devices, such as thyristors, with back-to-back junctions, to enable the termination of the opposing high-voltage junctions.

Simulation Example

The results of two-dimensional numerical simulations are provided in this section for the case of a drift region with doping concentration of 5×10^{13} cm^{-3} to gain further insight into the operation of the negative bevel junction termination. For this doping concentration, the breakdown voltage for the parallel-plane junction was found to be 3000 V with a depletion region thickness of 300 μm on the lightly doped side. A P-N junction with a highly graded P-region was achieved by using a surface doping concentration of 1×10^{17} cm^{-3} with a depth of 100 μm. These values are representative of the P-base region in high-voltage thyristors to provide its forward blocking capability. The simulations of the negative bevel termination were performed with various bevel angles ranging from 2.5° to 10°. All the structures had an oxide layer over the bevel surface as the passivation. The depletion layer width on the P-side of the junction was found to be about 30 μm. Thus, the simulated structure has a W_N/W_P ratio of 10.

The reduction of the maximum surface electric field obtained from the numerical simulations is shown in Fig. 3.50 for the various bevel angles. The surface electric

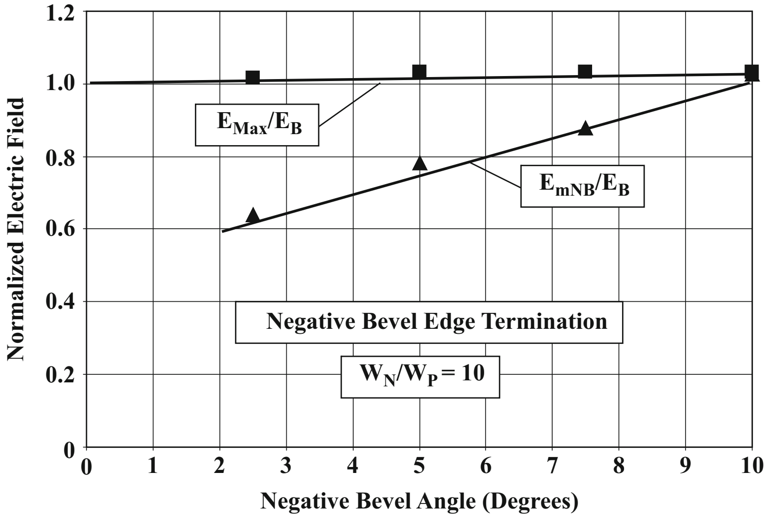

Fig. 3.50 Surface electric field reduction with a negative bevel termination

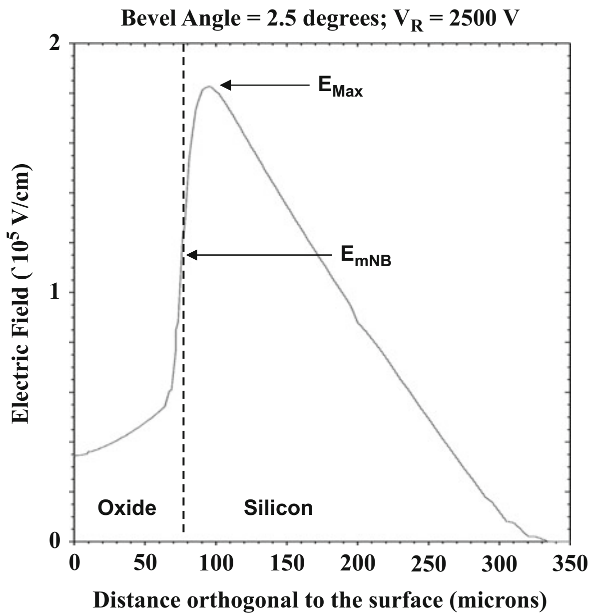

Fig. 3.51 Electric field profile in a negative bevel termination

field predicted by the simple analytical model is in the range of values obtained using the simulations. Despite the reduction of the surface electric field at the bevel for the shallow angles, the breakdown voltage was found to be reduced to about 85% of the parallel-plane value. This reduction is due to an enhanced electric field in the vicinity of the negative bevel. As an example, the electric field profile is shown in Fig. 3.51

along the vertical direction at a location where the surface electric field has its maximum value. It can be seen that the maximum electric field in the bulk (E_{Max}) is larger than at the surface of the negative bevel (E_{mNB}). This maximum electric field is slightly larger than the maximum electric field observed in the bulk parallel-plane portion of the P-N junction (E_{B}). This phenomenon is responsible for the reduction of the breakdown voltage with a negative bevel termination.

3.6.7 Etch Terminations

One of the earliest methods for the fabrication of multiple high-voltage devices on a single wafer relied upon etching a moat around the reverse blocking junction of each device as illustrated in Fig. 3.52. A variety of masking materials, such as black wax, photoresist, and metal, were utilized with etch solutions containing a mixture of nitric, hydrofluoric, and sulfuric acid. Although widely used for the manufacturing of products in the 1950s and 1960s, this approach fell out of favor due to the lack of control over the shape and depth of the moat. The deep contour of the moat was also a major problem for passivation of the junction.

It can be seen from the illustration of the moat etch termination in Fig. 3.52 that the surface at the edges of the junction approximates a 90° bevel angle. This results in a relatively high surface electric field at the termination producing poor stability in the breakdown voltage. This situation can be improved upon by creating a planar junction with the moat located to create an effective positive bevel. Two examples of this approach are illustrated in Fig. 3.53. In the first case, shown on the left-hand side, the moat intersects the planar junction producing a local positive bevel. This has been demonstrated to reduce the surface electric field [21]. The second approach, shown on the right-hand side in the figure, places the moat within the depletion region extending from the P-N junction. This is also equivalent to a positive bevel based upon its definition of more material being removed from the lightly doped side of the junction than the heavily doped side. Although this method for edge

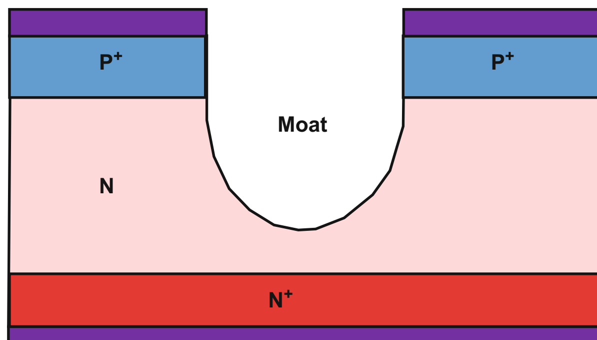

Fig. 3.52 Moat etch termination

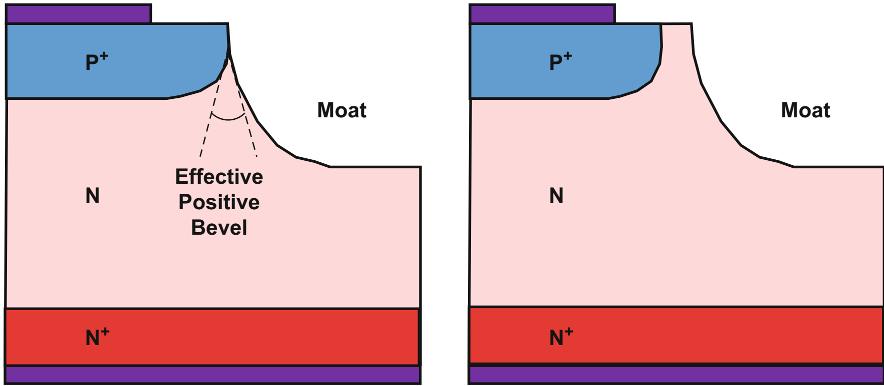

Fig. 3.53 Alternate moat etch terminations

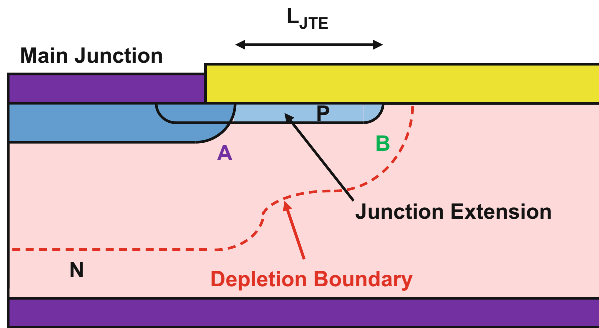

Fig. 3.54 Junction termination extension

termination is superior to the moat etch shown in Fig. 3.35, it is not commonly used in modern power devices because the wet chemical etching of silicon has fallen out of favor in fabrication facilities.

3.6.8 Junction Termination Extension

The bevel edge terminations rely upon the selective removal of charge from the two sides of the P-N junction at the edges. A complementary approach for altering the surface electric field at the edges is based upon selectively adding charge to the junction. This can be done by ion implantation of a P-type region at the edge of a planar P^+ diffusion as shown in Fig. 3.54. This P-type region has been named the *junction termination extension* or JTE region [22]. The charge within the P-type region can be precisely adjusted with the ion implant dose providing better control and uniformity over the charge at the edges of the junction than with the bevel

terminations while retaining a planar surface. This is advantageous for manufacturing multiple small power devices on a single wafer.

The charge within the JTE region must be precisely controlled to maximize the breakdown voltage. If the charge is small, it has little impact on the electric field distribution and the maximum electric field will occur at point A as in the case of the unterminated planar junction. This will result in a breakdown voltage limited by the cylindrical junction curvature as discussed earlier in the chapter. If the charge in the JTE is high, it will merely serve as an extension of the junction to point B with a smaller radius of curvature. This will result in a reduction of the breakdown voltage due to the enhanced curvature at the cylindrical junction located at point B. In order to reduce the electric field at the main junction at point A without encountering breakdown at point B at low reverse bias voltages, the charge in the JTE region must be such that it is completely depleted by the reverse bias.

For a homogeneously doped region, the charge within the depletion region is related to the doping concentration and maximum electric field by:

$$Q = \int_0^W qN_A dx = qN_A W_D = \varepsilon_S E_m \tag{3.80}$$

The maximum electric field at the junction becomes equal to the critical electric field when the junction reaches its breakdown voltage. Under these conditions:

$$Q_{OPT} = \varepsilon_S E_C \approx 2.07 \times 10^{-9} \mathrm{C/cm^2} \tag{3.81}$$

if a critical electric field of 2×10^5 V/cm is assumed for silicon. The corresponding dopant dose is 1.3×10^{12} cm^{-2} in the JTE region. If the dose for the P-type implant is chosen to produce this charge, the JTE region will become completely depleted at the breakdown condition. Since the entire JTE region is depleted, the electric field is distributed along the surface over the length (L_{JTE}) of the junction termination region. If the length of the JTE region is chosen to be much longer than the depletion width of the main junction, the surface electric field can be reduced to below that for a parallel-plane junction. Consequently, the breakdown voltage of this termination can approach that of an ideal parallel-plane junction.

In practice, the breakdown voltage for the junction termination extension has been found to be strongly dependent upon the charge of the ion-implanted JTE region. Although ion implant doses can be precisely metered, the charge in the JTE region can vary due to dopant segregation during annealing of the implant and the growth of the oxide layer for the passivation of the surface. In addition, the electric field distribution in the JTE region can be perturbed by the fixed oxide charge which can vary across the wafer. This can result in a variation of the breakdown voltage across the wafer as well as unstable behavior if mobile ions are introduced into the passivation during packaging of the die.

An elegant approach to improving the performance of the junction extension termination is by using multiple zones of ion-implanted regions at the edge of the main junction [23]. By using three zones with a charge reduction by a factor of 2×

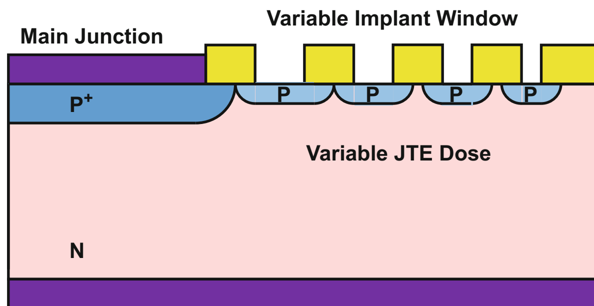

Fig. 3.55 Junction termination extension with variable lateral doping

when proceeding from the main junction toward the exterior, breakdown voltages of over 90% of the parallel-plane value have been reported. Although these three JTE zones could be fabricated by using three masking and implant steps, an elegant and less expensive approach uses a single mask with a variable window size when proceeding from the main junction to the exterior as illustrated in Fig. 3.55. The JTE dose decreases when proceeding away from the main junction because of the smaller effective doping concentration in the silicon in spite of using a single ion implantation step. The JTE zones can also be merged together by using a suitable annealing step to diffuse the dopant sideways between the windows.

Simulation Example

The results of two-dimensional numerical simulations are provided in this section for the case of a drift region with doping concentration of 3.8×10^{14} cm^{-3} to gain further insight into the operation of the junction termination extension. This doping concentration corresponds to that used earlier for the cylindrical junction and floating field ring examples. The breakdown voltage for the parallel-plane junction in this case was found to be 520 V with a depletion region thickness of 41 μm on the lightly doped side. The JTE region was created using a Gaussian doping profile with various P-type doses.

The breakdown voltage obtained using the two-dimensional numerical simulations are plotted in Fig. 3.56 as a function of the dose for the P-type dopant in the JTE region. These breakdown voltages were observed for the case of a JTE region length of 40 μm, which is equal to the width of the depletion region at breakdown for the parallel-plane junction. It can be seen that the breakdown voltage has a maximum value of about 90% of the parallel-plane junction at a JTE region dose of 1.3×10^{12} cm^{-2}. This optimum dose for the JTE region observed with the simulations is in remarkably good agreement with the optimum dose predicted by Eq. (3.80).

The change in the breakdown voltage with increasing dose in the JTE region can be understood by examination of the electric field profile within the JTE region. At low values for the dose, the electric field along the surface within the JTE region exhibits a maximum value at the edge of the main junction as shown in Fig. 3.57 for case of dose of 0.3×10^{12} cm^{-2}. For high values of the dose, the electric field along the surface within the JTE region exhibits a maximum value at the edge of the JTE region as shown in Fig. 3.57 for case of dose of 1.5×10^{12} cm^{-2}. When a dose of 1.1

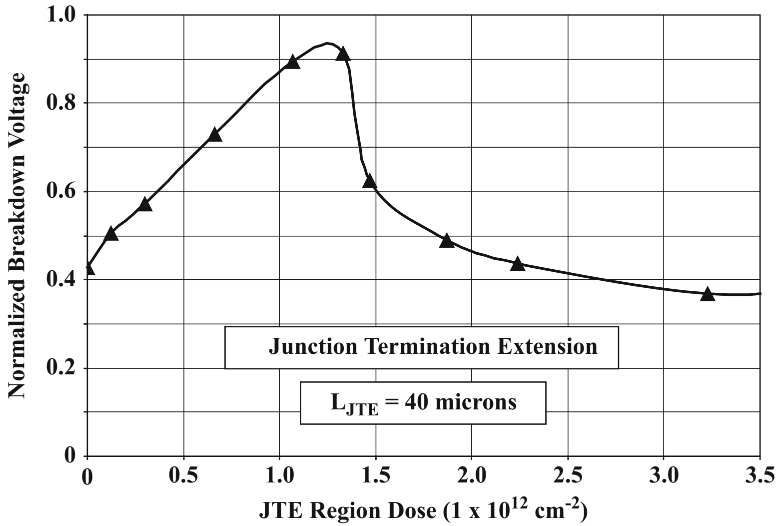

Fig. 3.56 Breakdown voltage obtained with the junction termination extension for a length of 40 μm

$\times\ 10^{12}\ \mathrm{cm}^{-2}$ is used, the electric field becomes relatively flat within the JTE region. This results in the highest breakdown voltage occurring at the optimum dose of 1.3 $\times\ 10^{12}\ \mathrm{cm}^{-2}$.

The length of the JTE region must also be sufficient to obtain the full benefits of reduction of the electric field along the surface at the edge of the planar junction. In order to illustrate this, the results of two-dimensional numerical simulations for the junction termination extension are shown in Fig. 3.58 for the case of a JTE dose of $1.1 \times 10^{12}\ \mathrm{cm}^{-2}$. A substantial increase in the breakdown voltage over that for the cylindrical junction is obtained when the length of the JTE region extends to the width of the depletion region for the parallel-plane junction at breakdown. An increase in the length of the JTE region much beyond this length does not produce further improvement in the breakdown voltage while consuming space at the edge of the device.

As discussed earlier, the breakdown voltage for the junction termination extension is sensitive to the presence of charge above the JTE region. The optimum charge in the JTE region has been shown to be $1.3 \times 10^{12}\ \mathrm{cm}^{-2}$. Unfortunately, the fixed oxide charge in thermally grown oxide over the silicon surface can be of this order of magnitude. If an optimum dose is used for the JTE region, the presence of the fixed oxide charge alters the electric field distribution along the surface at the JTE region producing a reduction of the breakdown voltage. In order to illustrate the influence of any surface charge on the breakdown voltage of the junction termination extension, two-dimensional numerical simulations were conducted for the case of the JTE structure with a dose of $1.1 \times 10^{12}\ \mathrm{cm}^{-2}$ and length of 40 μm with fixed oxide charge of $1 \times 10^{11}\ \mathrm{cm}^{-2}$. The breakdown voltage was found to be reduced from 465 V (89%

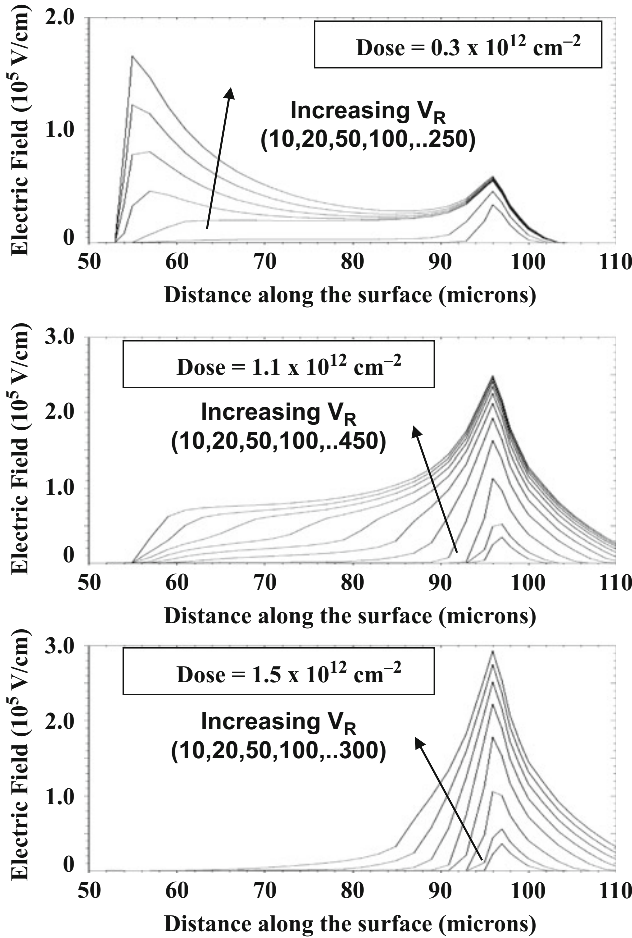

Fig. 3.57 Electric field profiles within the JTE region for three values of the JTE dose

of the breakdown voltage for the parallel-plane junction) without the fixed oxide charge to 450 V (86% of the breakdown voltage for the parallel-plane junction) with the fixed oxide charge. When the charge was increased to 3×10^{11} cm^{-2}, the breakdown voltage was reduced to 416 V (80% of the breakdown voltage for the parallel-plane junction).

These reductions of the breakdown voltage in the presence of the fixed oxide charge can be correlated with changes in the electric field distribution along the surface along the JTE region. The electric field profile is not significantly modified by the presence of a fixed oxide charge of 1×10^{11} cm^{-2} as shown in Fig. 3.59. However, when the charge is increased to 3×10^{11} cm^{-2}, the electric field at the edge of the JTE region is enhanced leading to the observed reduction of the breakdown voltage. Based upon these results, it can be concluded that the fixed

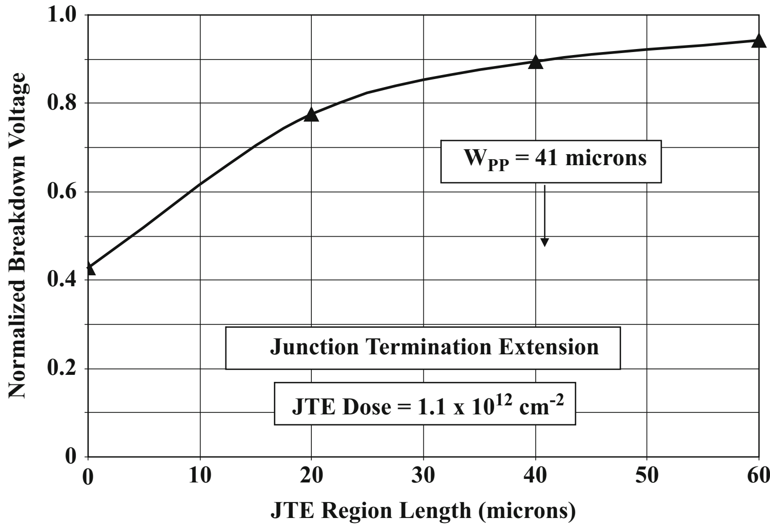

Fig. 3.58 Breakdown voltage obtained with the junction termination extension

oxide charge should be reduced to less than 1×10^{11} cm^{-2} during the passivation of the junction termination extension.

3.7 Open-Base Transistor Breakdown

In the previous sections of this chapter, the breakdown voltage of the P-N junction has been analyzed including the impact of enhanced electric fields at their terminations. These results have relevance to power devices with single blocking junctions, such as power rectifiers and power MOSFETs. In many other power devices, such as power thyristors and IGBTs, the structures contain back-to-back P-N junctions. The maximum voltage that can be supported by these structures becomes limited by *open-base transistor breakdown*. In this situation, the current generated by impact ionization is amplified by the gain of the bipolar transistor [24].

An open-base P-N-P transistor is illustrated in Fig. 3.60 with a positive bias applied to electrode on the right-hand side. The applied voltage produces a forward bias across the junction J_2, while junction J_1 becomes reverse biased. The reverse biased junction J_1 supports the voltage with the development of a depletion region in the N-base region. The boundary of the depletion region is indicated by the dashed line. The electric field profile for this case is shown in the middle of the figure. If the width (W_N) of the N-base region is large, breakdown will occur when the maximum electric field (E_m) becomes equal to the critical electric field for breakdown for the semiconductor. The breakdown voltage for this case is the same as that of the

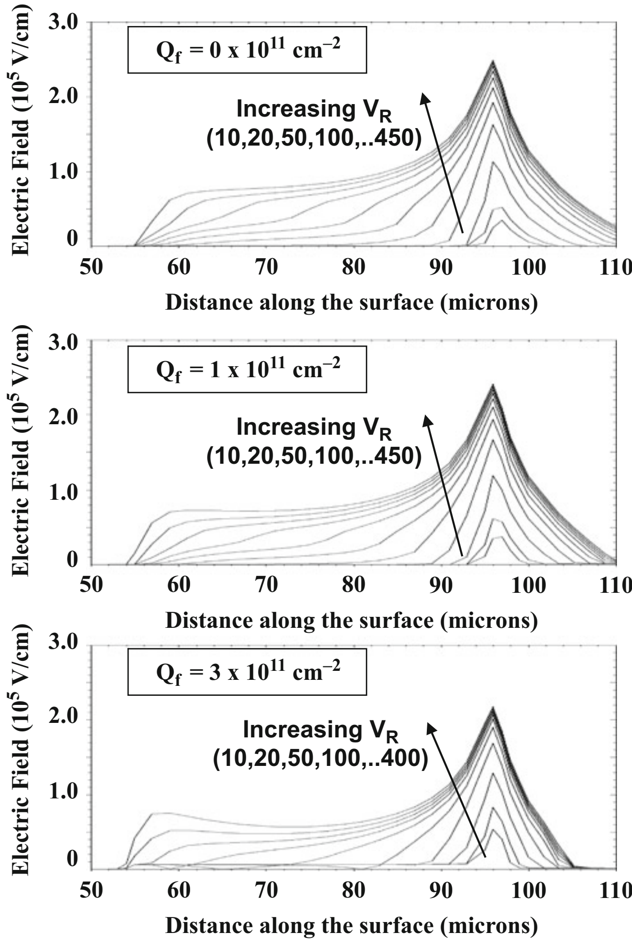

Fig. 3.59 Impact of fixed oxide charge on the electric field profiles within the JTE region

parallel-plane junction. This corresponds to the multiplication coefficient becoming infinitely large.

When the width (W_N) of the N-base region becomes shorter than the depletion width for breakdown for the parallel-plane junction, the breakdown voltage for the P-N-P transistor is reduced due to the reach-through effect. Open-base transistor breakdown is precipitated by the injection of holes from the forward biased junction J_2 with the current flow amplified by the gain of the bipolar transistor. The current due to the injected holes is indicated by the arrow labeled ($\gamma_E \alpha_T I_E$) at the depletion boundary and ($\alpha_{PNP} I_E$) at the collector junction J_1. Here, the emitter injection efficiency (γ_E) is close to unity, and the base transport factor (α_T) is less than unity, while the common emitter current gain (α_{PNP}) of the P-N-P transistor becomes larger than unity due to the onset of carrier multiplication at high bias voltages. In

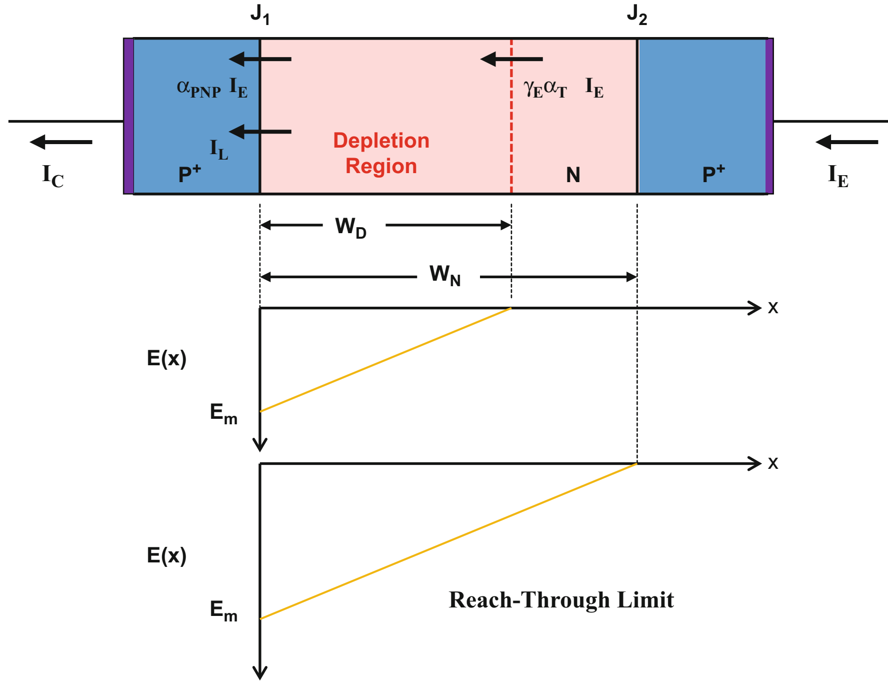

Fig. 3.60 Open-base transistor breakdown analysis

addition, the current due to the generation of carriers in the depletion region and the neutral region is indicated by the arrow labeled I_L in the figure. Using Kirchhoff's law:

$$I_C = \alpha_{PNP}.I_E + I_L = I_E \tag{3.82}$$

leading to

$$I_C = I_E = \frac{I_L}{(1 - \alpha_{PNP})} \tag{3.83}$$

Based upon this equation, it can be concluded that the current will become large when the current gain of the transistor approaches unity. The criterion for breakdown for the open-base transistor can therefore be written as:

$$\alpha_{PNP} = \gamma_E \alpha_T M = 1 \tag{3.84}$$

where M is the multiplication coefficient. These terms are discussed in detail in the chapter on bipolar power transistors. Due to the low doping concentration in the N-base region in symmetric blocking devices like thyristors and IGBTs to enable the support of high voltages, the injection efficiency can be assumed to be equal to unity. The base transport factor is less than unity as determined by the undepleted base width (W_N – W_D) and the minority carrier diffusion length (L_p):

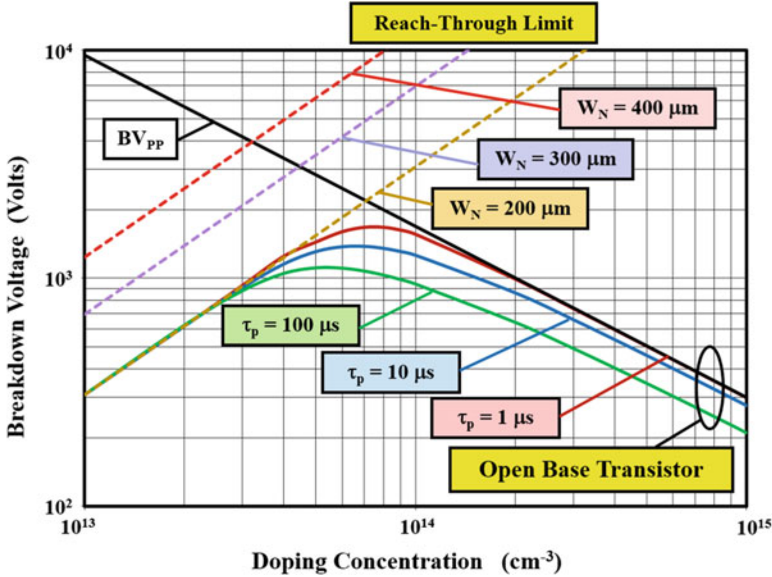

Fig. 3.61 Open-base transistor breakdown voltage

$$\alpha_T = \cosh^{-1}\left[\frac{W_N - W_D}{L_p}\right] \tag{3.85}$$

where W_D is the width of the depletion layer. The depletion region width is related to the applied reverse bias voltage by Eq. (3.15). The multiplication coefficient is also a function of the applied reverse bias as given by Eq. (3.9) for the case of a P^+/N diode. The breakdown voltage for the open-base transistor can therefore be determined by evaluation of the current gain as a function of the applied reverse bias to determine the voltage at which it becomes equal to unity.

As an example, the breakdown voltage for the open-base transistor is plotted in Fig. 3.61 for the case of an N-base width of 200 µm. Three values for the minority carrier (hole) lifetime are taken into consideration. In addition, the boundaries defined by pure avalanche breakdown (BV_{PP}) and the reach-through breakdown are included for comparison. The reach-through limit is defined as the voltage at which the depletion region width becomes equal to the width of the N-base region. This voltage is given by:

$$BV_{RT} = \frac{qN_D W_N^2}{2\varepsilon_S} \tag{3.86}$$

where N_D is the doping concentration in the N-base region. It is worth pointing out that the reach-through breakdown limit does not take into consideration avalanche multiplication at the reverse biased junction. Instead, it is assumed that when

the depletion region extends through the entire N-base region, any further applied bias produces the injection of minority carriers from the forward biased junction leading to the onset of high current flow.

From the figure, it can be observed that, on the one hand, when the doping concentration in the N-base region is low (less than 3×10^{13} cm^{-3} in the example), the open-base transistor breakdown voltage is limited by the reach-through phenomenon. On the other hand, when the doping concentration of the N-base region is high (more than 3×10^{14} cm^{-3} in the example with a low minority carrier lifetime), the open-base transistor breakdown voltage is limited by the avalanche multiplication phenomenon. The highest breakdown voltage is observed at a doping concentration of about 7×10^{13} cm^{-3} for this case with an N-base width of 200 μm. The open-base transistor breakdown voltage is always lower than the avalanche breakdown voltage with a greater reduction for cases with larger values for the minority carrier lifetime. For a minority carrier lifetime of 1 μs, the highest open-base breakdown voltage is 1670 V at an N-base doping concentration of 7×10^{13} cm^{-3} compared with an avalanche breakdown voltage of 2200 V at this doping concentration. This reduction must be taken into account during the design of devices, such as thyristors, which must exhibit both high forward and reverse blocking capability.

Simulation Example

The results of two-dimensional numerical simulations are provided in this section for the case of an N-base width of 200 μm to gain further insight into the operation of the open-base transistor. The breakdown voltages obtained using the two-dimensional numerical simulations are plotted in Fig. 3.62 as a function of the doping concentration in the N-base region for the case of a minority carrier lifetime of 10 μs. The

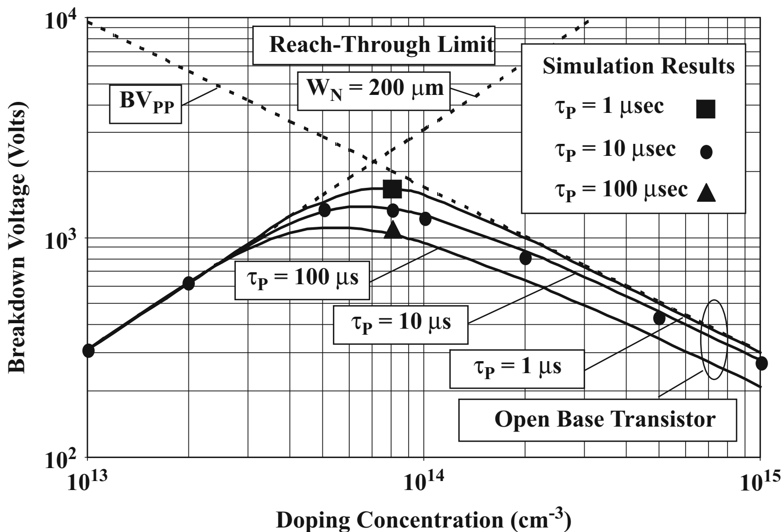

Fig. 3.62 Open-base transistor breakdown voltage for an N-base width of 200 μm

open-base transistor breakdown voltages predicted by the analytical model are in excellent agreement with the results of the simulations providing confidence in the model. The maximum breakdown voltage was found to be 1420 V at a doping concentration of 8×10^{13} cm^{-3} with the simulations compared with 1380 V obtained using the analytical model at a doping concentration of 7×10^{13} cm^{-3}. When the minority carrier lifetime was decreased to 1 μs in the simulations, the breakdown voltage was found to increase to 1600 V at a doping concentration of 8×10^{13} cm^{-3} compared with 1670 V obtained using the analytical model. When the minority carrier lifetime was increased to 100 μs in the simulations, the breakdown voltage was found to decrease to 1190 V at a doping concentration of 8×10^{13} cm^{-3} compared with 1110 V obtained using the analytical model.

3.7.1 Composite Bevel Termination

Power devices designed to support high voltages in the first and third quadrant of operation contain an open-base transistor structure with two back-to-back junctions. It is necessary to provide an edge termination for both of these junctions simultaneously. One approach to achieving a reduction of the surface electric field at both the junctions is by combining a positive bevel with a negative bevel as illustrated in Fig. 3.63. The depletion region boundary for the case of a positive bias applied to the anode, for operation in the first quadrant, is indicated in the figure by the dotted lines. In this case, the upper P-N junction J_1 becomes reverse biased leading to the extension of the depletion region downward toward junction J_2. This results in open-base transistor breakdown in the bulk region of the thyristor, which is smaller than the breakdown voltage at the negative bevel termination. In contrast, the depletion region boundary for the case of a negative bias applied to the anode, for operation in the third quadrant, is indicated in the figure by the dashed lines. In this case the lower P-N junction J_2 becomes reverse biased leading to the extension of the depletion region upward toward junction J_1. This also results in open-base transistor

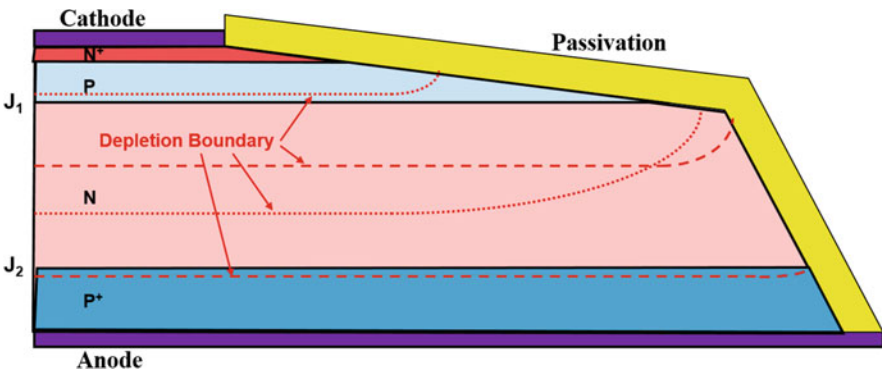

Fig. 3.63 Composite positive/negative bevel termination

breakdown in the bulk region of the thyristor, which is smaller than the breakdown voltage at the positive bevel termination. The design of the thyristor structure must take this into consideration.

3.7.2 Double-Positive Bevel Termination

Another approach to providing the edge termination for devices, such as thyristors designed to support high voltages in the first and third quadrant of operation with two back-to-back junctions, is by using a double-positive bevel. This concept relies on creating a local positive bevel for both of the high-voltage junctions. Two shapes for the double-positive bevel have been explored. The V-shape shown on the left-hand side of Fig. 3.64 can be produced by grit blasting at various angles to the edge of the wafer. The rounded shape shown on the right-hand side of the figure can be produced by using slurry on a wire that contacts the wafer edge, while the wafer is rotated about its center.

The depletion region boundary for the case of a negative bias applied to the anode, for operation in the third quadrant, is indicated in Fig. 3.65 by the dashed lines for the V-shaped double-positive bevel termination. In this case, the lower P-N junction J_2 becomes reverse biased leading to the extension of the depletion region upward toward junction J_1. At lower reverse bias voltages, the edge termination behaves as a positive bevel termination with the depletion region expanding at the edges. This reduces the electric field at the bevel surface. However, with increasing reverse bias, the depletion region eventually extends past the corner of the bevel (point A). Beyond this voltage, the angle of the bevel is reversed producing a local negative bevel. This alters the depletion region shape as indicated in the figure. In spite of this change in the bevel angle, the double-positive bevel termination has

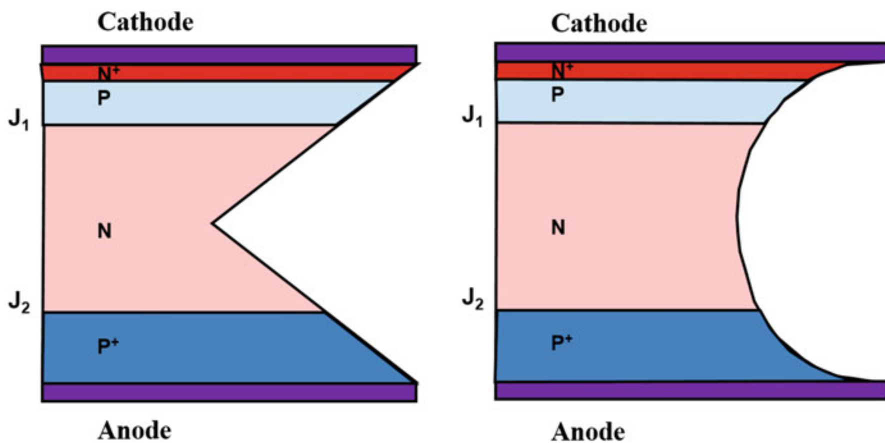

Fig. 3.64 Double-positive bevel terminations

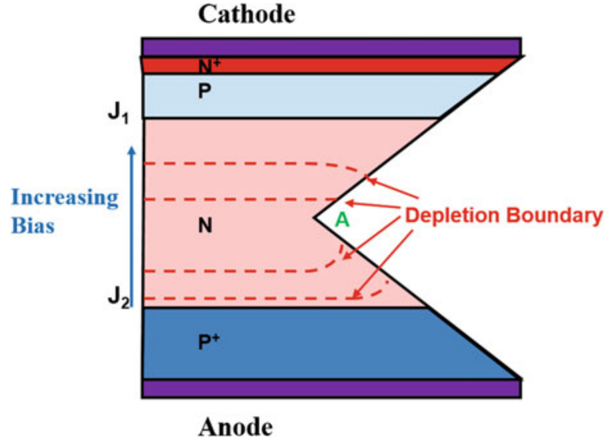

Fig. 3.65 Depletion layer extension in the double-positive bevel termination

been found [25] to suppress the surface electric field enabling breakdown to occur in the bulk. Two manufacturing difficulties that had to be overcome while developing this edge termination were to avoid breakage of the thin wafer edges created by the bevel and the passivation of the surface due to its concave topography.

Simulation Example

The results of two-dimensional numerical simulations are provided in this section for the case of the V-shaped edge termination to gain further insight into the operation of the double-positive bevel termination. The structure had an N-base width of 300 μm with a doping concentration of 5×10^{13} cm^{-3}. The diffused P^+ region had a junction depth of 50 μm. When a minority carrier lifetime of 1 μs was used, the open-base transistor breakdown voltage for the parallel-plane structure was found to be just above 2500 V for both polarities of the bias voltage. The double-bevel termination had a bevel angle of 45° in both directions. As expected, the breakdown voltages obtained for the double-bevel termination with both polarities of bias was found to be the same as that for the parallel-plane junction.

The electric field distribution within the double-positive bevel termination is shown in Fig. 3.66 at a bias of 2500 V. The electric field in the bulk exhibits the triangular shape with a maximum value of 1.85×10^5 V/cm located at the junction. The electric field along the bevel edge has a much lower value of 0.85×10^5 V/cm at the junction. The maximum electric field occurs in the vicinity of the corner of the bevel because of the change in the bevel angle from a positive value to a negative value. However, this electric field is also much lower than in the bulk ensuring a breakdown voltage equal to that for the open-base transistor with parallel-plane junctions. A much less reduction of the surface electric field has been reported for the rounded bevel termination [16].

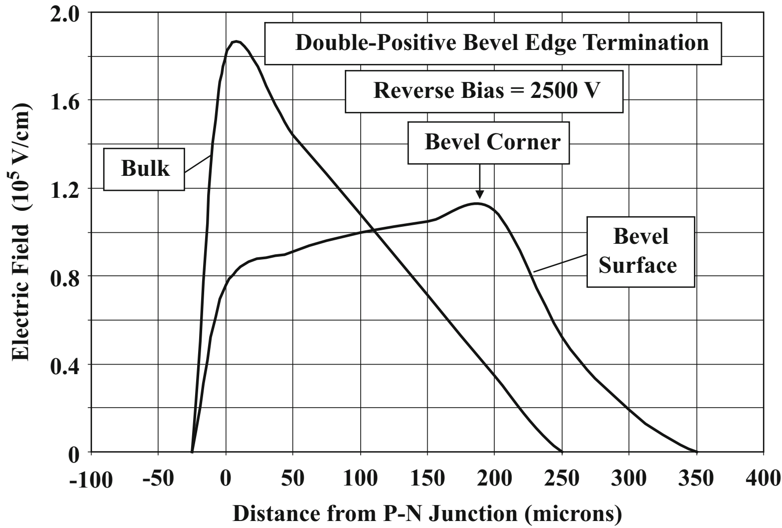

Fig. 3.66 Electric field profiles within the double-positive bevel termination

3.8 Surface Passivation

The leakage current and breakdown voltage of power devices can be compromised by poor surface passivation. The presence of mobile charge close to the semiconductor surface can lead to alterations of the electric fields at the edges during device operation producing changes in the breakdown voltage. Inadequate surface preparation of the silicon surface can lead to the presence of defects, such as dislocations, which adversely impact the leakage current due to a high density of deep levels in the bandgap. These defects can also initiate premature breakdown due to localized enhancements of the electric field.

For very high-voltage power devices, such as thyristors with bevel edge terminations, the commonly used surface passivation is with rubberized coatings or organic polymers [26]. The surface damage produced by the beveling process must be first removed by chemical etching of the surface, immediately followed by coating with silicone rubber or polyimide layers. The passivation layer is then cured. The devices are enclosed in a hermetically sealed package to minimize the presence of mobile ions and moisture.

For planar devices, it is commonplace to use silicon dioxide as the passivation layer at the edges. However, sodium and potassium ions are known to migrate through the oxide creating instability in the breakdown voltage. This can be prevented by covering the oxide with a silicon nitride or oxynitride film using plasma-enhanced chemical vapor deposition [27]. Another approach used for planar power devices is to utilize semi-insulating polycrystalline silicon (SIPOS) films

[28]. The resistivity of these films can be controlled by adjusting their oxygen content. Power bipolar transistors with breakdown voltages as high as 10,000 V have been fabricated using the SIPOS passivation method.

3.9 Silicon Carbide Edge Terminations

Silicon carbide rectifiers and power MOSFETs have been recently commercialized. Edge terminations that produce close to 100% of the ideal breakdown voltage had to be developed to maximize the performance of these devices. At first, the same edge termination concepts described in the previous sections of this chapter as used for silicon devices were utilized [29, 30]. Subsequently, improved edge terminations were created with breakdown voltages close to the ideal value. These types of edge terminations are discussed here.

3.9.1 *Argon-Implanted Edge Termination*

The argon-implanted edge termination for silicon carbide power devices is based up on creation of a high-resistivity region by the implantation of argon to generate deep levels within the bandgap. The high concentration of deep levels located near midgap forces the Fermi level away from the conduction band making the carrier concentration low within the argon-implanted portion. It was found that a dose of about 1×10^{15} cm^{-2} was able to raise the breakdown voltage very close to the ideal value corresponding to the doping concentration of the silicon carbide drift region [31, 32].

A larger leakage current is generated by this edge termination. This can be mitigated by using a finite length for the argon-implanted zone (L_{AIZ} in Fig. 3.67). A length (L_{AIZ}) of about five times the ideal depletion width at breakdown is sufficient to achieve close to the ideal breakdown voltage [33]. Since the leakage current is observed to continue to increase with the length of the zone, it is prudent to utilize a length of this magnitude.

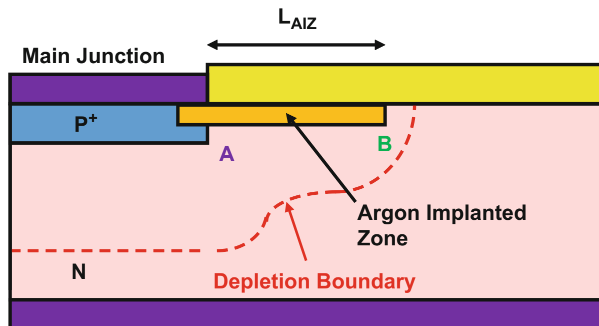

Fig. 3.67 Argon-implanted edge termination

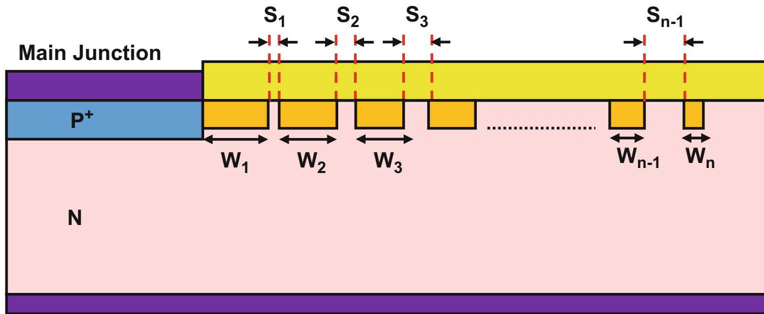

Fig. 3.68 Multiple-floating-zone junction termination extension

3.9.2 Multiple-Floating-Zone Junction Termination Extension

Multiple floating field rings were initially used as edge terminations for high-voltage silicon carbide devices [34]. This approach yields breakdown voltages below 80% of the ideal value [35]. Significantly larger breakdown voltages (90% of ideal value) can be achieved by using a two- or three-zone junction edge termination [36]. However, this approach requires two to three masking and ion implantation steps that add considerable cost to device fabrication.

An elegant solution is the fabrication of multiple floating zones with optimized dose for the P-type dopant similar to that used for the junction termination concept. This method, called multiple-floating-zone junction termination extension (MFZ-JTE) [37], is illustrated in Fig. 3.68. As illustrated in the figure, the sum of the width of each zone and the spacing (e.g., $W + S$) is kept constant while the width of the zone (W) is reduced by a constant factor α when proceeding away from the main junction. This creates a gradual reduction of the charge toward the edge of the termination resulting in the best electric field distribution and the highest breakdown voltage. A α value of 1.02 has been shown to produce nearly ideal breakdown voltage for the case of 36 and 72 zones if an optimum dose of 2×10^{13} cm^{-2} is used for the aluminum implant. This value corresponds to the optimum analytical dose obtained for 4H-SiC using the product of the dielectric constant and the critical electric field for breakdown.

3.9.3 Hybrid Junction Termination Extension

The hybrid junction termination extension is formed by combining a single-zone JTE region, floating field rings, and the multiple-zone JTE termination. The multiple-zone JTE termination described in the previous section is used for the

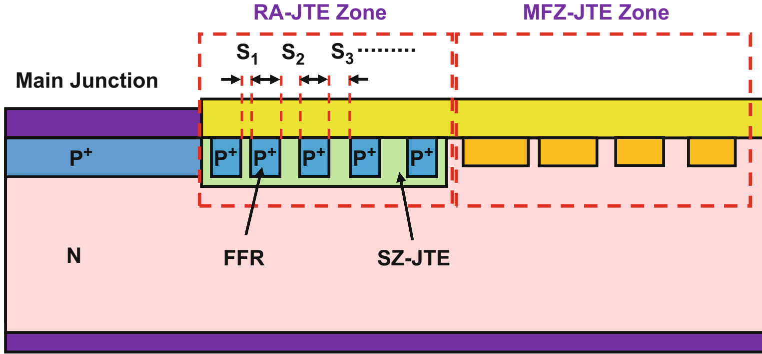

Fig. 3.69 Hybrid junction termination extension

outer portion of this hybrid termination. A single-zone JTE zone is added between the main junction and the MFZ-JTE portion. The single-zone JTE region is augmented with floating field rings as shown in Fig. 3.69 to create a ring-assisted JTE (RA-JTE) zone.

The spacing between the floating field rings in the RA-JTE zone is gradually increased ($S_1 < S_2 < S_3 \ldots$). An optimum dose of 1×10^{13} cm^{-2} is used for the JTE zone. A breakdown voltage of 5450 V was achieved with the hybrid JTE design for an epitaxial drift layer with doping concentration of 2×10^{15} cm^{-3} and thickness of 40 μm [38]. This is 99% of the ideal breakdown voltage of a parallel-plane junction. In comparison, the breakdown voltage for an optimized floating field ring design with 35 rings was only 4160 V.

3.9.4 Multiple Floating Field Ring Design

One of the commonly used edge termination designs for silicon carbide high-voltage devices makes use of a large number of floating field rings [39]. It is important to estimate the number floating field rings required to achieve a breakdown voltage close to the ideal parallel-plane value and to then obtain the space taken by the edge termination on the periphery of devices. A simplified analysis is provided here based up on the assumption of an approximately constant electric field (E_{M}) between the individual floating field rings as illustrated in Fig. 3.70. It is necessary to keep the value of this field significantly below the critical electric field (E_{CS}) for breakdown to avoid premature breakdown at the edge termination.

The voltage at the last (nth) floating field ring can be related to the voltage applied to the main junction (V_{M}) by:

$$V_{\mathrm{n}} = V_{\mathrm{M}} - (n\delta E_{\mathrm{CS}} W_{\mathrm{S}}) \tag{3.87}$$

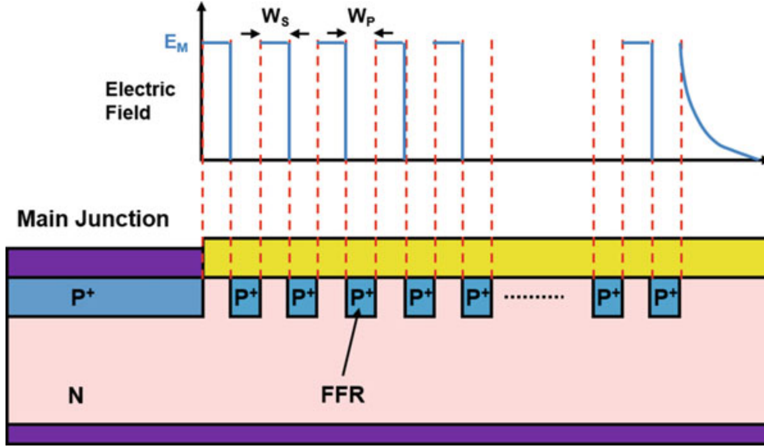

Fig. 3.70 Multiple floating field ring edge termination design

where E_{CS} is the electric field for impact ionization-induced breakdown at the surface, δ is desired reduction in the surface electric field, and W_S is the spacing between the floating field rings. The device breaks down at a main junction voltage of BV_{FFR} when the last ring has a voltage equal to the breakdown voltage of a cylindrical junction (BV_{CYL}). Using Eq. (3.88):

$$BV_{FFR} = BV_{CYL} + (n\delta E_{CS} W_S) \tag{3.88}$$

The number of floating field rings obtained from this equation is:

$$n = \frac{BV_{FFR} - BV_{CYL}}{\delta W_S E_{CS}} \tag{3.89}$$

Consider the case of a diode with breakdown voltage of 10 kV. Due to the shallow junction possible in SiC technology, the cylindrical breakdown voltage will be limited to only 20% of the parallel-plane breakdown voltage. The surface electric field for breakdown for SiC is about 1×10^6 V/cm. The number of rings is then found to be 80 under the assumption that the maximum electric field must be reduced to 50% of the critical electric field for breakdown at the surface and a space (W_S) of 2 μm between the rings.

The total width of the floating field ring edge termination is given by:

$$W_{FFR} = n(W_S + W_P) \tag{3.90}$$

where W_P is the width of each floating field ring. For the 10 kV design with 80 floating field ring, a total edge termination width is found to be 560 μm in this case. This is much greater than the parallel-plane breakdown depletion width of about 80 μm. Devices with 10 kV breakdown voltage have been reported using 100 floating field rings with a total width of 900 μm for the termination region [39].

3.9.5 Orthogonal Positive Bevel Termination

Silicon carbide devices with symmetric blocking capability are needed for AC circuit applications such as circuit breakers. A high blocking voltage can be achieved for these devices in the first quadrant of operation by using the designs described above. An elegant method to achieve high blocking voltage capability in the third quadrant has been demonstrated by using the orthogonal positive bevel edge termination [40].

The positive bevel edge termination has been used to make silicon high-voltage thyristors with large reverse blocking capability. For these devices, the positive bevel is formed by cutting the edge of the entire silicon wafer that comprises single-power devices at a positive bevel angle as previously discussed in Sect. 3.6.6. This method cannot be implemented for silicon carbide devices which have a small size with many devices located on a single wafer. The orthogonal positive bevel is formed for the SiC devices by cutting the wafers using a V-shaped sawing blade in orthogonal directions [40] similar to the usual sawing of dies apart using a vertical cut. A top view of the wafer at the edge of single chip is illustrated in Fig. 3.71 together with the cross section at the bottom of the figure. It has been demonstrated that the positive bevel increases the breakdown voltage close to the ideal parallel-plane breakdown voltage if the surface of the bevel is etched to remove the saw damage. The orthogonal positive bevel edge termination was subsequently used to create the first symmetric blocking SiC GTO with reverse blocking capability of 8 kV [41].

The orthogonal bevel has been used to create an edge termination that occupies less chip area by formation of the junction termination extension along the beveled edge surface [42]. A 1-min RTA anneal at 1000 °C in N_2O ambient after the aluminum JTE ion implant was necessary to reduce the leakage current. Breakdown

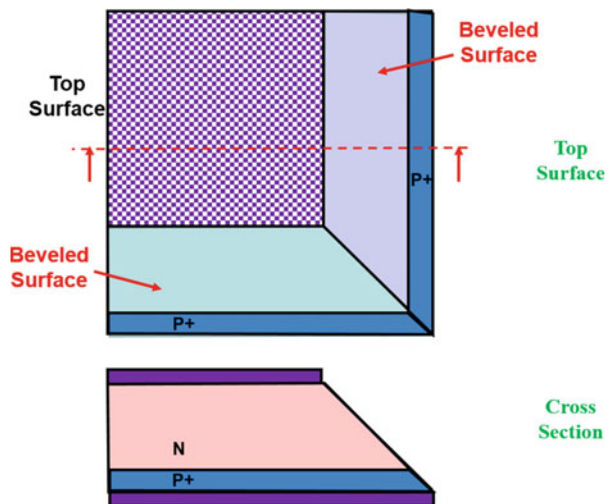

Fig. 3.71 Orthogonal positive bevel edge termination

voltage of 95% of the ideal parallel-plane value was experimentally obtained with a 45° bevel angle. The width of the edge termination on the top surface is reduced by three times compared with the conventional JTE edge termination. A detailed comparison of the beveled edge-based terminations with other edge termination approaches has been quantified by numerical simulations and experimental confirmation [43].

3.10 Summary

A relatively high breakdown voltage is the most distinguishing feature for a power device. This chapter has provided the criteria for the design of the breakdown voltage for typical P-N junction diodes that are representative of the internal structure of power devices. In practical structures, the breakdown voltage can be drastically reduced by the enhancement of the electric field at the edges of the devices. Various methods to suppress this electric field enhancement have been analyzed in this chapter. For devices with areas that are a small fraction of the wafer area, the most attractive edge terminations utilize planar junctions. For high-current devices fabricated using an entire wafer, it is possible to bevel the edge to reduce the electric field and ensure bulk breakdown.

Problems

3.1 Compare the impact ionization coefficient obtained using Baliga's formula to that for electrons and holes in silicon at an electric field of 2×10^5 V/cm.

3.2 Compare the impact ionization coefficient obtained using Baliga's formula to that for holes in 4H-SiC at an electric field of 2×10^6 V/cm.

3.3 Calculate the parallel-plane breakdown voltage for silicon abrupt P-N junctions at drift region doping concentrations of 1×10^{13} cm^{-3}, 1×10^{14} cm^{-3}, 1×10^{15} cm^{-3}, and 1×10^{16} cm^{-3}.

3.4 Calculate the parallel-plane breakdown voltage for 4H-SiC abrupt P-N junctions at drift region doping concentrations of 1×10^{14} cm^{-3}, 1×10^{15} cm^{-3}, 1×10^{16} cm^{-3}, and 1×10^{17} cm^{-3}.

3.5 Calculate the maximum depletion layer width at breakdown for silicon abrupt P-N junctions at drift region doping concentrations of 1×10^{13} cm^{-3}, 1×10^{14} cm^{-3}, 1×10^{15} cm^{-3}, and 1×10^{16} cm^{-3}.

3.6 Calculate the maximum depletion layer width at breakdown for 4H-SiC abrupt P-N junctions at drift region doping concentrations of 1×10^{14} cm^{-3}, 1×10^{15} cm^{-3}, 1×10^{16} cm^{-3}, and 1×10^{17} cm^{-3}.

3.7 Compare the critical electric field at breakdown for silicon and 4H-SiC abrupt P-N junctions with the same breakdown voltage of 1000 V.

3.8 Compare the ideal specific on-resistance for the drift region in silicon and 4H-SiC devices with the same breakdown voltage of 1000 V.

3.9 Calculate the width of the drift region for a silicon punch-through diode to achieve a breakdown voltage of 1000 V if the drift region doping concentration is 2×10^{13} cm^{-3}.

3.10 Calculate the width of the drift region for a 4H-SiC punch-through diode to achieve a breakdown voltage of 1000 V if the drift region doping concentration is 1×10^{15} cm^{-3}.

3.11 Calculate the breakdown voltage for a cylindrical junction termination with a depth of 3 μm for a silicon drift region with doping concentration of 1×10^{14} cm^{-3}.

3.12 Calculate the breakdown voltage for a spherical junction termination with a depth of 3 μm for a silicon drift region with doping concentration of 1×10^{14} cm^{-3}.

3.13 Calculate the breakdown voltage for a junction termination using the single optimally located floating field ring with a depth of 3 μm for a silicon drift region with doping concentration of 1×10^{14} cm^{-3}.

3.14 Determine the spacing for the single optimally located floating field ring in the previous problem. What is the mask dimension required for this design?

3.15 Determine the normalized surface electric field for a positive bevel termination with an angle of 45°.

3.16 Determine the normalized surface electric field for a negative bevel termination with an angle of 3° if the ratio of the depletion layer widths on the lightly doped side to the heavily doped side of the junction is 10.

3.17 Determine the optimum charge for the junction termination extension in a silicon device.

3.18 Determine the optimum charge for the junction termination extension in a 4H-SiC device.

3.19 Calculate the breakdown voltage for an open-base silicon transistor with a drift region doping concentration of 5×10^{13} cm^{-3} and thickness of 300 μm if the low-level lifetime is 10 μs. Compare this value to the avalanche breakdown voltage and the reach-through breakdown voltage.

3.20 Determine the impact of changing the drift region doping concentration to 2×10^{13} cm^{-3} in the previous problem.

References

1. Fulop W (1967) Calculation of avalanche breakdown of silicon P-N junctions. Solid State Electron 10:39–43
2. Baliga BJ (2010) Advanced power MOSFET concepts. Springer-Science, New York
3. Baliga BJ (2006) Silicon carbide power devices. World Scientific Publishing Company, Singapore
4. Raghunathan R, Baliga BJ (1999) Temperature dependence of hole impact ionization coefficients in 4H and 6H SiC. Solid State Electron 43:199–211
5. McIntyre RJ (1966) Multiplication noise in uniform avalanche diodes. IEEE Transactions on Electron Devices ED-13:164–168

6. Ghandhi SK (1977) Semiconductor power devices. Wiley, New York, p 39
7. Howard NR (1962) Avalanche multiplication in silicon junctions. J Electronic Control 13:537–544
8. Bauer FD (2011) Compact high-precision models for silicon p-n step junction avalanche-breakdown voltages. IEEE Transactions on Electron Devices 58:658–663
9. Sze SM, Gibbons G (1966) Effect of junction curvature on breakdown voltage in semiconductors. Solid State Electron 9:831–845
10. Temple VAK, Adler MS (1975) Calculation of the diffusion curvature related avalanche breakdown in high voltage planar P-N junctions. IEEE Trans Electron Dev ED-22:910–916
11. Baliga BJ, Ghandhi SK (1976) Analytical solutions for the breakdown voltage of abrupt cylindrical and spherical junctions. Solid State Electron 19:739–744
12. Van Overstraeten R, DeMan H (1970) Measurements of the ionization rates in diffused silicon P-N junctions. Solid State Electron 13:583–608
13. Koa YC, Wolley ED (1967) High voltage planar P-N junctions. Proc IEEE 55:1409–1414
14. Adler MS et al (1977) Theory and breakdown voltage of planar devices with a single field limiting ring. IEEE Trans Electron Dev ED-24:107–113
15. Baliga BJ (1990) Closed form analytical solutions for the breakdown voltage of planar junctions terminated with a single floating field ring. Solid State Electron 33:485–488
16. Grove AS, Leistiko O, Hooper WW (1967) Effect of surface fields on the breakdown voltage of planar silicon P-N junctions. IEEE Trans Electron Dev ED-14:157–162
17. Baliga BJ (1979) Deep planar gallium and aluminum diffusions in silicon. J Electrochem Soc 126:292–296
18. Cornu J (1973) Field distribution near the surface of beveled P-N junctions of high voltage devices. IEEE Trans Electron Dev ED-20:347–352
19. Adler MS, Temple VAK (1978) Maximum surface and bulk electric fields at breakdown for planar and beveled devices. IEEE Trans Electron Dev ED-25:1266–1270
20. Adler MS, Temple VAK (1976) A general method for predicting the avalanche breakdown voltage of negative beveled devices. IEEE Trans Electron Dev ED-23:956–960
21. Temple VAK, Baliga BJ, Adler MS (1977) The planar junction etch for high voltage and low surface fields in planar devices. IEEE Trans Electron Dev ED-24:1304–1310
22. Temple VAK (1977) Junction termination extension: a new technique for increasing avalanche breakdown voltage and controlling surface electric fields at P-N junctions. IEEE International Electron Devices Meeting, Abstract 20.4, pp 423–426
23. Stengle R, Gosele U (1985) Variation of lateral doping – a new concept to avoid high voltage breakdown of planar junctions. IEEE International Electron Devices Meeting, Abstract 6.4, pp 154–157
24. Herlet A (1965) The maximum blocking capability of silicon Thyristors. Solid State Electron 8:655–671
25. Cornu J, Schweitzer S, Kuhn O (1974) Double positive bevel: a better edge contour for high voltage devices. IEEE Trans Electron Dev ED-21:181–184
26. Verderber RR et al (1970) Passivation of high power rectifiers. IEEE Trans Electron Dev ED-17:797–799
27. Blaha RE, Fahrner WR (1976) Passivation of high breakdown voltage P-N-P structures by thermal oxidation. J Electrochem Soc 123:515–518
28. Matsushita T et al (1976) Highly reliable high voltage transistors by use of the SIPOS process. IEEE Trans Electron Dev ED-23:826–830
29. Bhatnagar M et al (1993) Edge terminations for SiC high voltage Schottky rectifiers. IEEE International Symposium on Power Semiconductor Devices and ICs. pp 89–94
30. Palmour JW et al (1997) Silicon carbide for power devices. IEEE International Symposium on Power Semiconductor Devices and ICs. pp 25–32
31. Alok D, Baliga BJ, McLarty PK (1994) A simple edge termination for silicon carbide with nearly ideal breakdown voltage. IEEE Electron Dev Lett 15:394–395

32. Alok D, Raghunathan R, Baliga BJ (1996) Planar edge termination for 4H-SiC devices. IEEE Trans Electron Dev 43:1315–1317
33. Alok D, Baliga BJ (1997) SiC device edge termination using finite area argon implantation. IEEE Trans Electron Dev 44:1013–1017
34. Sheridan DC et al (2000) Simulation and fabrication of high voltage 4H-SiC diodes with multiple floating guard ring termination. Silicon Carbide Relat Mater – 1999, Mater Sci Forum 338-342:1339–1342
35. Li X et al (2000) Theoretical and experimental study of 4H-SiC junction edge termination. Silicon Carbide Relat Mater – 1999, Mater Sci Forum 338-342:1375–1378
36. Perez R et al (2005) Planar edge termination design and technology considerations for 1.7 kV 4H-SiC PiN diodes. IEEE Trans Electron Dev 52:2309–2316
37. Sung W et al (2011) A new edge termination technique for high voltage devices in 4H-SiC – multiple floating zone junction termination extension. IEEE Electron Dev Lett 32:880–882
38. Sung W et al (2016) A new ideal edge termination technique for 4500V 4H-SiC devices: the hybrid junction termination extension. IEEE Electron Dev Lett 37:1609–1612
39. Ryu SH et al (2006) 10 kV, 5 A 4H-SiC Power DMOSFET. IEEE International Symposium on Power Semiconductor Devices and ICs. p 1–4
40. Huang X et al (2013) SiC symmetric blocking terminations using orthogonal positive bevel termination and junction termination extension. IEEE International Symposium on Power Semiconductor Devices and ICs, Paper WB-P4. pp 179–182
41. Sung W et al (2015) The first demonstration of symmetric blocking SiC gate turn-off (GTO) Thyristor. IEEE International Symposium on Power Semiconductor Devices and ICs. pp 257–260
42. Sung W, Huang AQ, Baliga BJ (2016) Bevel junction termination extension – a new edge termination technique for 4H-SiC high voltage devices. IEEE Electron Dev Lett 36:594–596
43. Sung W, Baliga BJ, Huang AQ (2016) Area-efficient bevel-edge termination techniques for SiC high-voltage devices. IEEE Trans Electron Dev 63:1630–1636